Master Thesis

**Convection-Enhanced Delivery
for the treatment of brain cancer**

Lambride Chryso

*DEPARTMENT OF MECHANICAL AND
MANUFACTURING ENGINEERING*

MAY 2021

UNIVERSITY OF CYPRUS
DEPARTMENT OF MECHANICAL AND MANUFACTURING ENGINEERING

Convection-Enhanced Delivery
for the treatment of brain cancer

Lambride Chryso

<u>Advisor</u>
Prof. Triantafyllos Stylianopoulos

The Master Thesis was submitted for partial fulfillment of the requirements for obtaining the degree of Mechanical and Manufacturing Engineering of Mechanical and Manufacturing Engineering Department

May 2021

Acknowledgements

First and foremost, I wish to express my deepest gratitude to my thesis advisor Prof. Triantafyllos Stylianopoulos for his generous support, guidance and encouragement throughout the process of conducting this thesis. He steered me in the right direction and without his participation and input, this project could not have been successfully conducted. I thank Prof. Vasileios Vavourakis and Prof. Andreas Kyprianou for their comments and ideas that greatly improved this Thesis. I also thank the PhD candidates Andreas Hadjigeorgiou and Constantinos Harkos for their guidance and feedback.

Lastly, I would like to thank my family and friends for their continuous love and support.

Abstract

Effective cancer treatment, especially in the brain, remains a formidable challenge in the field of oncology. Convection-enhanced delivery (CED) is an innovative and promising local drug delivery method for brain cancer, overcoming the challenges of conventional methods. The project develops a mathematical and computational model for brain cancer treatment to predict the drug concentration distributions, applying engineering and physical sciences principles to medicine. In this in silico study, an individualized, three-dimensional finite element model of the brain is used to investigate the CED for the treatment of brain cancer. The model incorporates nonlinear biomechanics, which describes the distribution of the drug concentrations using diluted species transport equations and applying the theory for hindered transport of rigid solutes. The aim of this work is to investigate the drug concentration during CED of different drug sizes by changing the pathophysiological conditions of the tumor tissue. To achieve this, different drug and tumor vessel wall pore sizes and various tumor interstitial space hydraulic conductivity values have been considered to account for a range of drug physicochemical and tumor microenvironment properties. To our knowledge, this present work reports for the first time directly how the size of the vascular wall pores and that of the therapeutic agent affect drug distribution during and after CED. These predictive outcomes provide further and useful insights of the spatial distribution and the average drug concentration in the tumor towards an effective treatment of brain cancer.

Contents

Figures

Annexes

Chapter 1

1.1 Physical microenvironment of tumor tissues

By applying principles of engineering and physical sciences to oncology, the mechanical behaviour of tumor tissues and all their components becomes more understandable. Therefore, more effective approaches for treatments are more likely to be found. Physical forces have a crucial role in tumor progression and cancer treatment. The mechanics of the solid and fluid components of a tumor affect the tissue microenvironment, making it difficult and sometimes infeasible to transfer therapeutic agents [1].

1.1.1 Abnormalities of the tumor mechanical microenvironment

Tumor tissues contain cancer cells and a diversity of stromal cells, including fibroblasts and cells of the immune system. They also consist of the extracellular matrix (ECM) which is the non-cellular solid component of tissue and provides structural integrity and it is a mean for biochemical signaling. Common tumor ECM is comprised of collagen and hyaluronan (HA). Additionally, the blood vessels pass through the tumor tissue, bringing nutrients and oxygen, while the lymphatic vessels are located at the tumor periphery, removing fluid, macromolecules and cells [1, 2]. Figure 1.1A illustrates the components and microenvironment of the tumor tissue.

The biochemical and physical microenvironments of tumors are dynamic. They evolve during tumor growth, progression and treatment and are strongly associated with abnormalities in the tumor vasculature and extravascular components. During tumor growth, adequate supply of oxygen and nutrients is required, increasing the demand for blood vessels. One of the mechanisms to meet this demand is known as angiogenesis in which new blood vessels sprout from existing ones. Another mechanism is non-angiogenetic growth in which cancer cells grow around pre-existing vessels. Nevertheless, the blood vessels resulting from angiogenesis are abnormal in structure

and function. Specifically, they are focally hyperpermeable due to large intracellular and intercellular openings. Simultaneously, the uncontrolled proliferation of cancer cells in the confined space of the host tissue causes an accumulation of compressive forces, which are stored in solid structural elements of the tumor and surrounding tissue. Due to these compressive forces, the intratumoral blood and lymphatic vessels can be compressed. As a results, a desmoplastic reaction can be induced in some tumor types, resulting in the excessive production of tumor ECM. In normal tissues, the lymphatic system has a crucial role to manage tissue fluid pressure by removing plasma that has leaked from the blood vessels. However, the present of solid stresses inside tumor tissues causes a dysfunctional lymphatic system, as existing lymphatic vessels collapse and new ones are not able to form [1].
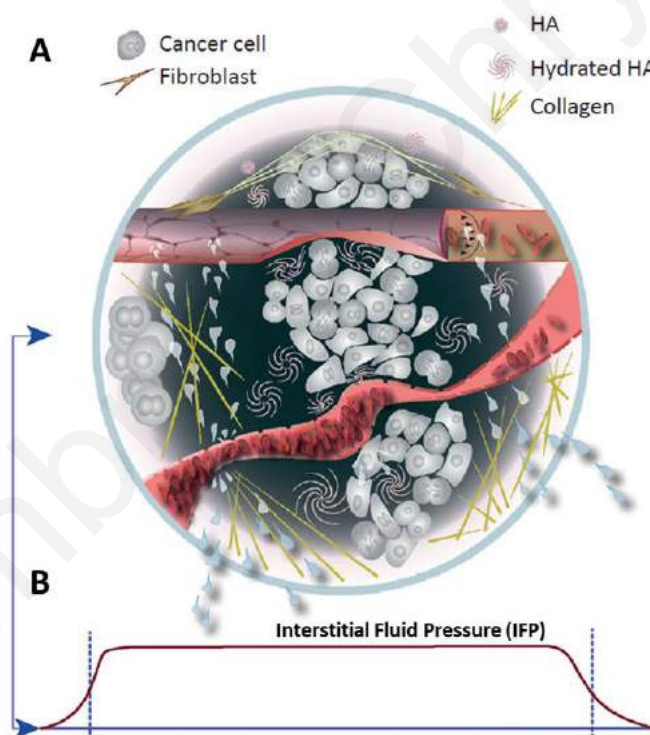
Figure 1.1: (A) Microenvironment of tumor tissues. **(B) S**chematic presentation of interstitial fluid pressure (IPF) elevation. [1]

These vascular deficiencies cause an increase in interstitial fluid pressure (IFP). The IFP is the extravascular hydrostatic pressure within the tumor and is elevated throughout the tumor and drops precipitously in the tumor margin, Figure 1.1B. The main reason for IPF elevation is the combination of the focal hyperpermeability of the tumor blood vessels and dysfunctional lymphatic system in the tumor. Specifically, the hyperpermeability of blood vessels permits plasma leakage into the tumor interstitial space and this fluid cannot be drained by the non-functional lymphatic vessels.

Moreover the dense ECM prevents this fluid from easily escaping from the tumor into the surrounding normal tissue. Besides, plasma leakage along with blood vessels compression can decrease blood flow within the vessels, making large intratumoral regions hypoperfused. Taken together, elevated IPF and hypoperfusion are the main physiological barriers to the transport of drugs through the tumor vasculature, across the tumor blood vessel wall into the tumor interstitial space, and through the interstitial space of the tumor. Figure 1.2 summarizes the effects of the tumor abnormalities on tumor perfusion and IFP, and the related barriers to drug transport. Additionally, hypoperfusion creates hypoxia, enhancing tumor progression in many ways. More specifically, hypoxia reduces immune cell activity, increases the metastatic potential of cancer cells, reduces the effectiveness of radiation therapy and immunotherapy, and forces cancer cells to adopt a more drug-resistant 'stem-cell' like phenotype. Consequently, by understanding the mechanisms of genesis and evolution of mechanical forces in tumors and the obstacles they present, better and more effective treatments can be achieved [1, 2].
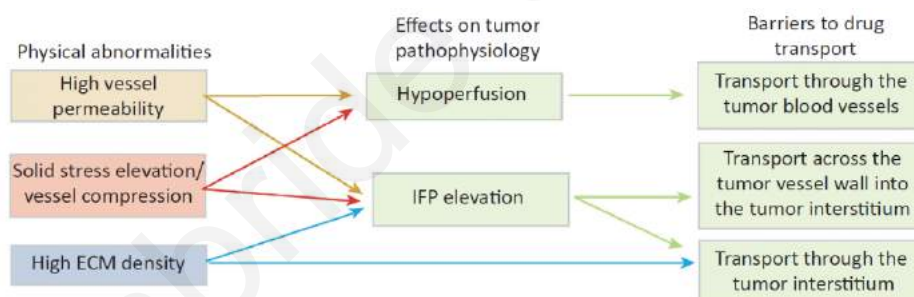
Figure 1.2: Effects of abnormalities of the tumor mechanical microenvironment on tumor pathophysiology and drug delivery. [1]

Over the last two decades, using *in silico* and *in vivo* studies, the mechanisms and the effects of IPF elevation on drug delivery have been identified. The normalization of the tumor vasculature and microenvironment is a promising approach for cancer treatment. The tumor tissue normalization can decrease both fluid pressure (IFP) and solid stress to improve drug delivery [1-3]. Studies have demonstrated that the dense extracellular matrix may contribute to the drug resistance of a solid tumor by preventing the penetration of therapeutic agents [3]. Reengineering the tumor microenvironment (vessel normalization and decompression) alleviate hypoxia and cancer heterogeneity is overcomed. By repairing the abnormalities of the tumor vessels, hypoxia can be relieved, and thus the tumor tissue heterogeneity reduces, delaying progression and improving cancer treatment results [2].

1.1.2 Drug transport mechanisms

The failure of cancer treatment is largely owing to insufficient amount of therapeutic agents in the tumor tissue. Due to the complexity and abnormality of the solid tumor tissue, the therapeutic agents do not reach all the cancer cells in adequate amounts to kill them without causing adverse effects. The abnormal microenvironment is characterized by impaired perfusion, hypoxia, low pH, and elevated fluid and solid stresses. Using a systemic administration, drugs have to flow though the vascular system to reach the tumor area, then they should pass across the tumor vessel wall to the tumor interstitial space, and eventually penetrate the interstitium to reach cancer cells. Typically, transport across the tumor vessel wall (transvascular transport) and within the tumor interstitial space (interstitial transport) can be achieved either through diffusion owing to concentration gradients, or through convection due to pressure gradients, Figure 1.3. Transvascular convection is governed by the hydraulic conductivity of vessel walls, whereas transvascular diffusion is defined by the vascular permeability. On the other hand, interstitial convection and diffusion depend on the interstitial space hydraulic conductivity and the diffusion coefficient, respectively [1].
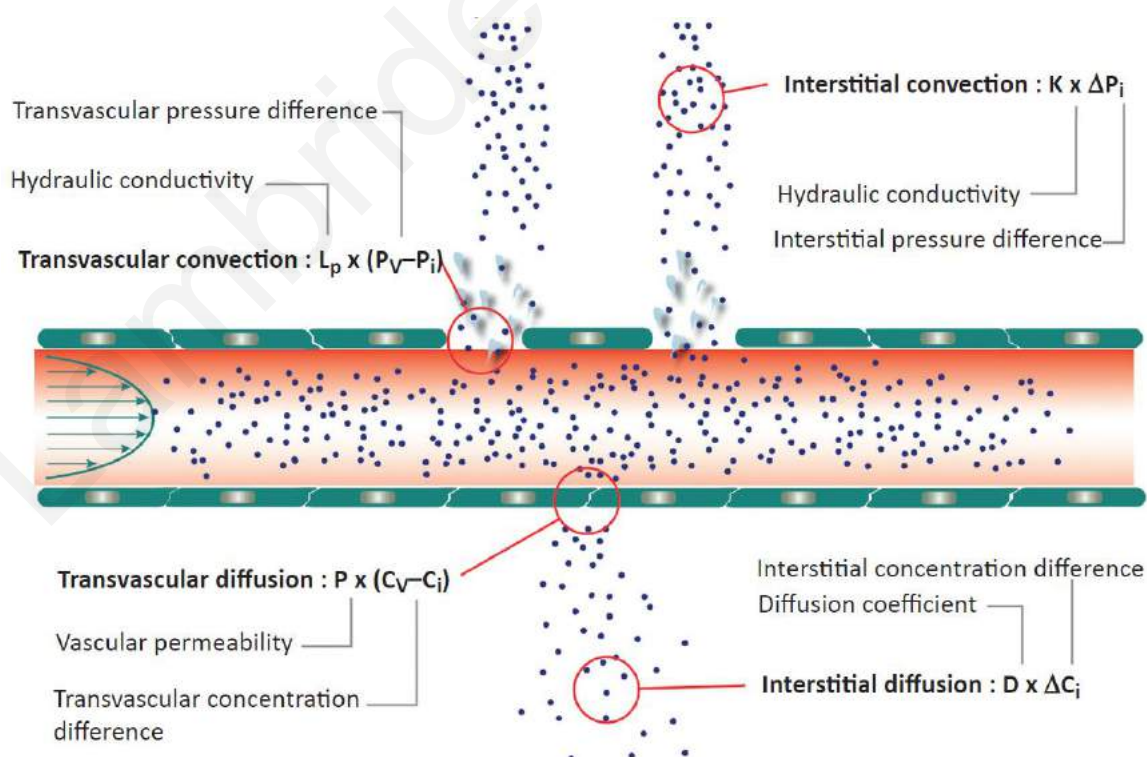
Figure 1.3: Transvascular and interstitial drug transport mechanisms. [1]

The extravasation of drugs from the blood vessels can be through diffusion and convection. The convectional part of drug transport across a vessel wall is based on

Starling principle. When both convection and diffusion are present, the total net transvascular drug flow is given by the Staverman-Kedem-Katchalsky equation, Equation 1.

$$J = PS_v(C_v - C_i) + L_pS_v(1 - \sigma_f)[(p_v - p_i) - \sigma(\pi_v - \pi_i)]C_v \qquad \text{Equation 1}$$

where J is the flow rate of drugs crossing the vessel, P is the vascular permeability of the drug, S_v is the vascular density, C_v-C_i is the concentration difference of the drug between the vascular and interstitial space, L_p is the hydraulic conductivity of the vessel wall, p_v-p_i is the difference between microvascular and interstitial fluid pressure, σ_f is the reflection coefficient, σ is the osmotic reflection coefficient and π_v-π_i is the colloidal osmotic pressure (oncotic pressure) difference across the wall [1, 4, 5].

The hydraulic conductivity of microvascular walls (L_p) describes the ease with which the fluid flows through the vessel wall pores and depends on the size of pores and the fraction of the vessel surface occupied by pores. The effective vascular permeability (P) is a measure of how easily solutes cross the blood vessel wall and is a function of the drug properties, *i.e.*, size, charge and configuration, and the vessel wall structure, *i.e.*, pore size, charge and arrangement. The reflection coefficients depend on the ratio of solute diameter to pore diameter.

Furthermore, IFP is uniformly elevated within the tumor interior and may be as high as the microvascular pressure due to the tumour tissue abnormalities. This leads to the elimination of the fluid pressure gradients, resulting in a negligible transvascular pressure difference, as well as interstitial pressure difference. Therefore, drug transport through convection is limited, rendering diffusion the main drug delivery mechanism. The convection mechanism is significant only at the margin of the tumor, causing transvascular and interstitial fluid flow. Another effect of the leaky nature of tumor vessels is the elevation of the oncotic pressure in the tumor interstitial space, which is similar with that in the blood plasma. As a result, the oncotic pressure difference is insignificant in tumor tissues [1].

Apart from transvascular drug transport, drugs can penetrate and be distributed within the interstitial space and this transportation is also governed by both diffusion and convection, Equation 2.

$$\frac{\partial C_i}{\partial t} + \nabla \cdot (-D\nabla C_i + \boldsymbol{u}C_i) = R \qquad \text{Equation 2}$$

where C_i is the drug concentration in interstitial space, $\boldsymbol{u}$ is the interstitial fluid velocity (IFV), D is the diffusion coefficient and R is a term representing degradation or cellular uptake. The fluid velocity depends on spatial changes in the interstitial fluid pressure and the hydraulic conductivity of the interstitial space (K) and is described by the Darcy's law: $\boldsymbol{u}=K\nabla p_i$, where p_i is the interstitial fluid pressure. The interstitial space hydraulic conductivity controls the flow through the interstitium, since it is a measure of how easily interstitial fluid flows though the network of pores formed from matrix structures and cells [1, 6].

As mentioned above, the abnormalities of the tumor microenvironment affect the delivery of therapeutic agents. Due to the vessel compression, hyperpermeability, abnormal morphology and organization, poorly perfused tumor vessel can be occurred, restricting the transport of cells, molecules and particles through the vasculature, *i.e.*, vascular transport. Moreover, the sharp gradient of IFP in the tumor periphery causes fluid to exit which can carry drugs, growth factors and cancer cells. These transporters could then enter the functional lymphatic system found at the tumor periphery, promoting metastasis. The dense tumor ECM hinders the diffusion and penetration of large macromolecules and nanoparticles, and as a result a homogeneous drug distribution is difficult to be achieved in the tumor interstitial space. The drug pharmacokinetics depends on the drug physical properties, such as size, shape, charge, binding affinity, and metabolism or degradation [1].

1.2 **B r a i n C a n c e r**

1.2.1 Overview of brain cancer

Effective cancer treatment, especially in brain region, remains a formidable challenge in the field of oncology. Although important advances have been made in treatment of many other cancer types, brain cancer constitute an unsolved clinical problem [7]. In recent years, significant improvements have been made in surgery, imaging and adjuvant therapy. However the average prognosis for glioblastoma multiforme (GBM) is only about 13 months, with a 2-year survival rate of 27%, and a 5-year survival rate of 5.1% [8]. Brain cancer is also the most common cause of cancer-related death in children aged 0-14 years [7].

Treatment of brain cancer remains a challenge despite the rapid development of several modalities, such as chemotherapy, immunotherapy, and targeted therapy, pharmaceutical agents [9]. Numerous obstacles are associated with the treatment of neurological diseases. One of the most significant barriers is the blood-brain barrier (BBB) which is responsible for the gap between scientific progress and the improved outcomes of several neurological diseases [8].

Specifically, the BBB between the blood circulation and the central nervous system (CNS) plays a key role in maintaining the stability of the microenvironment [10]. Due to its unique anatomic structure, it regulates homeostasis of the CNS by forming a tightly regulated neurovascular unit that includes endothelial cells, pericytes and astrocytic endfeet, which together maintain normal brain function [10, 11]. BBB exists along the cerebral capillaries and isolates the systemic circulation from the cerebral parenchyma, providing protection to brain cells. Apart from its protective role, BBB hinders the delivery of systemic therapies into brain tumours [7, 8, 11]. During tumor progression, the tumor vasculature becomes increasingly heterogeneous and BBB is disrupted, known as blood-tumor barrier (BTB). The BTB is generally considered leakier than the BBB. Its heterogeneous permeability to small and large molecules as well as heterogeneous perfusion contribute to suboptimal drug accumulation in brain tumor. Moreover, in the case where drug is administered intravenously, the higher drug concentration is accumulated within brain tumors as compared with the unaffected brain. The aforementioned observation as well as the detection of brain tumor markets

in the circulation are the evidence for BBB disruption. In glioblastoma, the BTB displays abnormal barrier features which disrupt vascular integrity during tumor progression.

It is worth noting that the BBB is one of the rate-limiting factors in clinically effective therapy [11]. Since the BBB inhibits the diffusion of solutes into the extracellular space of the CNS, high drug concentrations should be given systemically in order to achieve sufficient amounts in the extracellular space. This can result in significant toxicities that should be avoided. Additionally, systemic administration or drug administration directly into the intrathecal or intraventricular space, is limited by blood-cerebrospinal fluid (CSF) barrier which acts similarly to the BBB. Consequently, achieving adequate therapeutic drug concentrations in targeted area of the brain is becoming increasingly challenging [8, 12].

1.2.2 Treatments of brain cancer

Early detection and remediation play a key role for positive prognosis. The detection and treatment of intracranial cancer are still difficult in the earliest stages of tumor due to the tumor location. The tumor is adjacent to or within anatomical structures vital for basic motor, cognitive, reflexive and other functions. Treatment of brain tumors has historically consisted of surgery followed by adjuvant therapy such as radiation therapy, chemotherapy and photodynamic therapy. Therefore, the standard therapy for newly diagnosed malignant gliomas includes surgical resection followed by combined radiotherapy/chemotherapy and adjuvant chemotherapy. Surgical and adjuvant therapy for brain tumors has been improved, however each treatment modality has limiting factors. The multidisciplinary approach currently used in the treatment of malignant brain tumors does not produce a significant improvement in patient outcome [7, 13].

It was remarkable that most chemotherapeutic agents have a low therapeutic index, they are toxic and can also affect healthy cells. This leads to severe systemic side effects, resulting in morbidity or mortality in the patient. As mentioned, the BBB is able to exclude a wide range of anticancer agents, restring the chemotherapy treatment of brain cancer. Furthermore, a combinational chemotherapy which uses more than one drug, is a common practice in clinical oncology, however, cancer cells often develop multi-drug resistance. In addition, the combination of chemotherapy and radiotherapy

has been successfully applied to adult brain tumors, but it also has significant treatment-related morbidity. Towards a more effective chemotherapy treatment of brain cancer, there have been ongoing efforts to develop specific delivery methods designed to overcome the BBB. Proper combination of these methods and the molecular-targeting approach should be key factors for achieving an improved therapeutic efficacy [7].

Various strategies have been developed to circumvent the barriers presented by the BBB for drug delivery. The basic principle of all strategies is to deliver and achieve high concentrations of drugs in the desired areas of the brain by bypassing the BBB in various ways. Generally, the advanced approaches can be classified into invasive and non-invasive which present selective advantages and limitations. Some of the invasive techniques are interstitial wafers and implant, intrathecal administration, and convection-enhanced delivery. Examples for non-invasive approaches are chemical modification of drugs, temporary disruption of the BBB and carrier/receptor-mediated delivery [7, 14]. Intravenous administration is restricted by the present of the BBB, while local delivery results in limited parenchyma penetration [12]. Therefore, in addition to the systemic application, local and convection-enhanced delivery applications have been established [13].

Moreover, the effectiveness of cancer detection and treatment can be achieved by providing effective concentrations of contrast or therapeutic agents selectively to the tumors. The utilization of nanoparticles has emerged as a potential vector for brain delivery, due to its excellent engineerability and non-toxicity. The construction of multi-functionality on a single nanoplatform can provide specific tumor detection, treatment and monitoring. Recent advances have been made in nanoparticle-based detection and treatment of brain cancer [7].

1.3 Convection-enhanced delivery

Neurodegenerative diseases of CNS are usually treated by systemic delivery of large molecular weight drugs either orally or intravenously. Nevertheless, the BBB prevents most of these molecules from entering the interstitium, making systemic delivery methods highly ineffective [15]. Innovative therapies have been recently developed, overcoming the challenges posed by the BBB with limited systemic toxicity and achieving promising results in the effective treatment of the brain cancer.

1.3.1 Overview of convection-enhanced delivery for brain cancer

Convection-enhanced delivery (CED) is a promising local drug delivery method for brain cancer. CED have been developed by Edward Oldfield and his scientific group at the National Institute of Health in the early 1990s [16]. The technique was suggested as a method to transport drugs which are either limited by the BBB or are too large to diffuse effectively. CED is a broadly applicable technique that can be used to deliver a variety of drugs for a diversity of diseases, such as glioblastoma multiforme (GBM), Parkinson's disease and Alzheimer's disease [8]. CED offers important advantages over systemic chemotherapy [7, 17], as it can bypass the BBB by direct infusion into the interstitial space of the brain tumor *via* surgically placed catheters [9, 14]. CED involves a minimal invasive surgical exposure of the brain [14] and can reach the peritumoral region and beyond [17]. Thereby, it allows the delivery for a diverse type of therapeutic agents without a molecular cut-off [14, 17]. Targeted delivery and perfusion of deep brain targets can be achieved both near and downstream of the infusion site [8].

CED represents a new option for the chemotherapy and an innovative solution for the treatment of brain tumors. It becomes a more frequent experimental treatment option in the management of malignant brain tumors, especially in recurrent GBM [13]. CED method involves the implantation of one or more catheters and utilizes a positive pressure gradient created by an infusion pump to inject drugs through the catheter and into the interstitial space of the solid tumor tissue, as shown Figure 1.4. Continuous positive-pressure bulk flow can be occurred, and thus conventional and novel therapeutic agents can be delivered. By applying this method, the therapeutic agents can be administered directly to a specific targeted area, enabling the distribution of large volumes of high drug concentrations with minimum systemic toxicity. Compered to

low-flow delivery methods based on diffusion, high-flow microinfusion, like the CED technique, offers much larger distribution volumes, spreading the drug through the tumor tissue. Application of the therapeutic agent through CED results in the extent of convection, which leads to a faster coverage of larger tumor volumes and also to the risk reduction of possible side effects. These major advantages of CED offer great potential for more efficient brain tumor treatments [12, 13, 15, 17, 18].
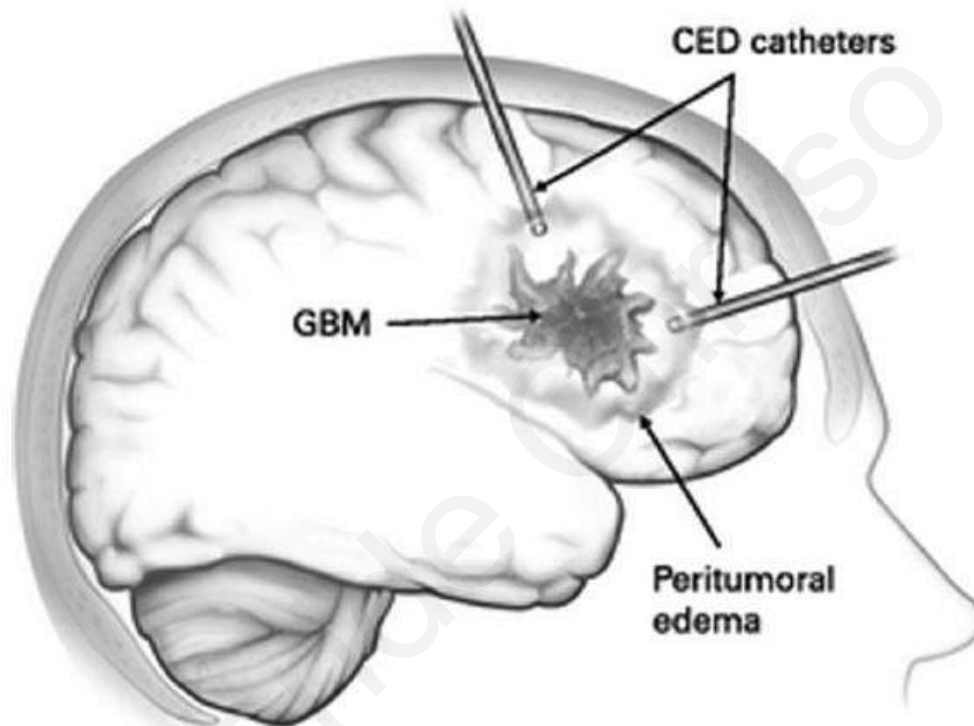
Figure 1.4: Convection-enhanced delivery (CED) with implantation one or more catheters for brain tumor treatment. [8]

Apart from bypassing the BBB, the major goal of CED is to provide safe, targeted, homogeneous delivery of a therapeutic agent to cancer cells, reaching great local therapeutic concentrations and reducing as much as possible systemic side effects and neurotoxicity [13]. This novel therapeutic technique holds considerable promising in neurological drug delivery. However, CED is a complex and demanding process that is governed by key parameters which limit success to clinical outcomes [18, 19]. There are several technical and physiological parameters directly related to transport by convection and especially to the volume distribution, and the control of the backflow mechanism. One of them is the brain region where the tumor is located. The tissue properties, i.e., permeability, hydraulic conductivity, isotropic or anisotropic diffusion, change depending on the brain region, e.g. gray and white matter. Additionally,

placement, size and design of the catheter are very important and crucial technical parameters of CED method for preventing backflow, reflux, mechanical tissue damage and other complications. Likewise, the infusion rate plays a key role for successful CED method. The injection flow is a critical parameter to create convection and is depended on cannula size used. In most cases, the optimal infusion rate is the one which allows the therapeutic volume to be delivered in the shortest duration without any associated reflux. The higher the infusion rate and catheter diameter used, the greater the reflux induced [8, 18, 20]. To understand and thus address these limitations, it is necessary to conduct further clinical and simulation CED studies.

Regarding to CED clinical studies, two approaches have been widely investigated. The one of them involves tumor resection and thus catheters are implanted in the brain surrounding the resected tumor cavity. This approach is used in the NeoPharm PRECISE trial. The second approach includes catheters that are placed directly into the non-resectable tumor. This method of delivery is used in the TransMID trial [13].

1.3.2 *Literature Review of in silico CED studies*

Several *in silico* studies have been developed to understand better the mechanism and limitations of CED method. Støverud *et al.* created a numerical model which includes both transport of a therapeutic agent and tissue deformation. Their study combine patient-specific parameters and brain structure using a poro-elastic model, with information about the anatomy, heterogeneities, and anisotropy of the tissue from diffusion tensor imaging (DTI) [21]. Moreover, many computational studies have been employed to investigate a catheter design and placement, infusion flow rate and how drug concentration distribution, backflow and reflux are affected. [15, 22]. Evaluation and prediction of therapy distribution in tumor based on the optimal catheter placement location can provide guidelines for effectively treating brain tumors using CED [22]. Studies focus on the engineering of a novel backflow-free catheter which provides means of allowing the therapeutics to reach an increased concentration to the site of delivery and a more predictable distribution that is critical for patient care [15]. A three-dimensional (3D) human brain finite element model of backflow was developed to study the influence of anatomical structures during flow-controlled infusions [23].

In addition, Linninger and his scientific group proposed patient-specific model, offering a concise tool for selecting suitable infusion parameters systematically based

on advanced imaging techniques and experimental data. The predictions of drug distribution were based on rigorous transport principles and the estimation of heterogeneous anisotropy properties were determined by DTI data. They found that regional and structural heterogeneity of the brain tissue influence drug distribution in CED method. Comparing the model prediction and experiments, they also examined the effect of drug concentration, catheter design and placement on the concentration distribution and the penetration depth of drug. The predictions were confirmed with experimental trials, indicating that for a given flow rate, thinner catheters lead to larger distribution volumes [24, 25].

Furthermore, Zhan and co-workers have carried out a series of computational and mathematical studies. In 2017, they examined drug transport under different CED operating conditions (infusion rate, solution concentration and infusion site location). Their modeling predications suggest that drug penetration can be improved by raising the infusion rate and the infusion solution concentration, and high drug concentration can be achieved mainly around the infusion site. [26]. In the same year, Zhan and his research team studied CED of six chemotherapeutic drug based on multi-physical model. They conclude that the drug non-uniform penetration and accumulation in brain tumor are strongly dependent on the drug physicochemical properties. They also suggest that drug carriers in nanoscale and diagnostic ultrasound can be applied with CED for improving the delivery outcomes [27]. A year later, Zhan and co-workers investigated the CED of liposome encapsulated doxorubicin under various delivery conditions. They found that compared to the direct infusion of doxorubicin, the drug accumulation and penetration can be importantly enhanced by using liposome-CED method. This treatment can be improved by either increasing the liposome solution concentration and infusion rate, decreasing the liposome vascular permeability, or placing the infusion site in tumor with sparse microvasculature [28]. Zhan *et al.* conduct additional studies for the effects of tissue permeability and drug diffusion anisotropy on the CED of different drugs. They propose that the permeability affected insignificantly the therapy distribution volume, however it can alter the drug spatial distribution [29]. Additionally, Zhan *et al.* developed a multiphysics 3D model for CED of anti-angiogenic and cytotoxic drugs into a brain tumor. Prediction outcomes show that anti-angiogenesis can slightly enhance the bulk flow of interstitial fluid, but could considerably reduce the fluid loss from the blood circulatory system [30].

1.4 Project aim

This Master Thesis focuses on the biomechanical and biotransport aspect of convection-enhanced delivery (CED), which is an innovative and promising technique for efficient delivery of drugs to brain tumors. The project develops a mathematical and computational model for brain cancer treatment to predict the drug concentration distributions, applying engineering and physical sciences principles to medicine.

In this *in silico* study, an individualized, three-dimensional (3D) finite element (FE) model is used to investigate the CED for treatment of brain cancer. The 3D FE model incorporates nonlinear biomechanics, describing the distribution of the drug concentrations using diluted species transport equations and applying the theory for hindered transport of rigid solutes through liquid filled pores to describe drug transport across the tumor vessel walls. The aim of this work is to investigate the drug concentration during CED of different drug sizes by changing the pathophysiological conditions of the tumor tissue. To achieve this, therapeutic agents of 1, 20 and 60 nm in diameter and vessel wall pores of tumor tissue with diameters 50, 100 and 150 nm have been considered. More specifically, the vascular wall pore size defines the vessel wall hydraulic conductivity, whereas the relative size of the drug to the vessel wall pore size determines the permeability of the drug across the vessels. The vascular permeability controls the diffusion of the drug through the pores. Further, the impact of the hydraulic conductivity of the tumor interstitial space on the distribution of the drug is extensively investigated. To our knowledge, this present work reports for the first time directly how the size of the vessel wall pores and that of the therapeutic agent affect the drug distribution during and after CED. These predictive outcomes provide further and useful insights of the spatial distribution and the average drug concentration in the tumor towards an effective treatment of brain cancer.

Chapter 2

2.1 Three-dimensional reconstruction and model extraction from MR images

Magnetic resonance (MR) images of a healthy adult male, as shown in Figure 2.1, are used to create an individualized, three-dimensional (3D) finite element (FE) model of the brain. The MR images are acquired from our previous study [31] and are reused in this work to demonstrate *in silico* CED biomechanics. The commercial software Simpleware ScanIP (version 6.0; Synopsys, Mountain View, USA) is used for the three-dimensional reconstruction of brain geometry. Specifically, two masks are first generated from the MR images using Simpleware's "threshold" operation, which selects each pixel according to its brightness. The darker areas consist the mask of the gray matter, whereas the brighter regions comprise the mask of the white matter in the brain. These masks are two different domains of the resulting 3D brain geometry. Then, the "island removal" and "cavity fill" operations are used to eliminate small unconnected parts of the masks and fill any gaps of the model, respectively. Smoothing is performed using the "Gaussian smoothing" operation. The 3D brain geometry is eventually created and exported in a COMSOL-compatible geometry file.
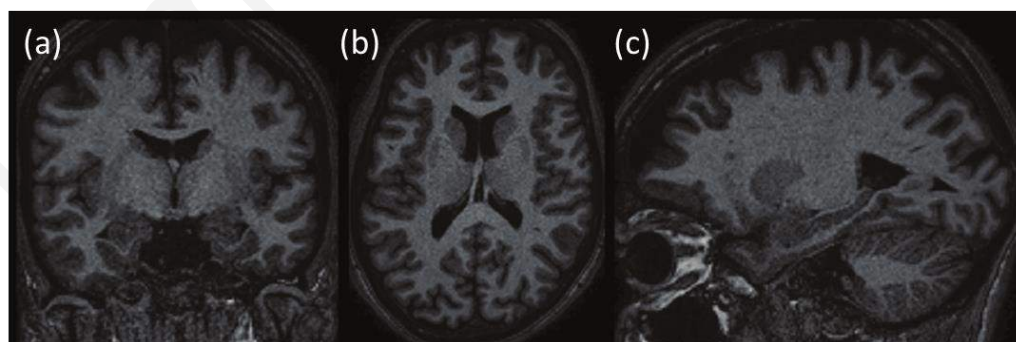
Figure 2.1: MR images of a healthy adult male: (a) coronal plane, (b) axial plane and (c) sagittal plane.

The 3D brain geometry is imported to the commercial FE software COMSOL Multiphysics (version 5.5; COMSOL Inc., Burlington, MA, USA). Subsequently, a sphere with radius 6mm and a cylinder with outer radius 1.5mm are formed inside the brain geometry to represent tumor and catheter domains, respectively. The sphere

(tumor) is located in the white matter inside the parietal lobe of the left cerebral hemisphere. Hence, the 3D brain geometry for CED therapy consists of four domains, i.e., gray matter, white matter, tumor, and catheter. Next, the FE mesh is created though the "free tetrahedral" and "boundary layer" operations to form an optimal mesh with boundary layers at the interfaces between the geometry domains. Figure 2.2 illustrates the individualized 3D FE brain model applied to CED therapy simulations. All simulations are carried out using the commercial FE software COMSOL Multiphysics.
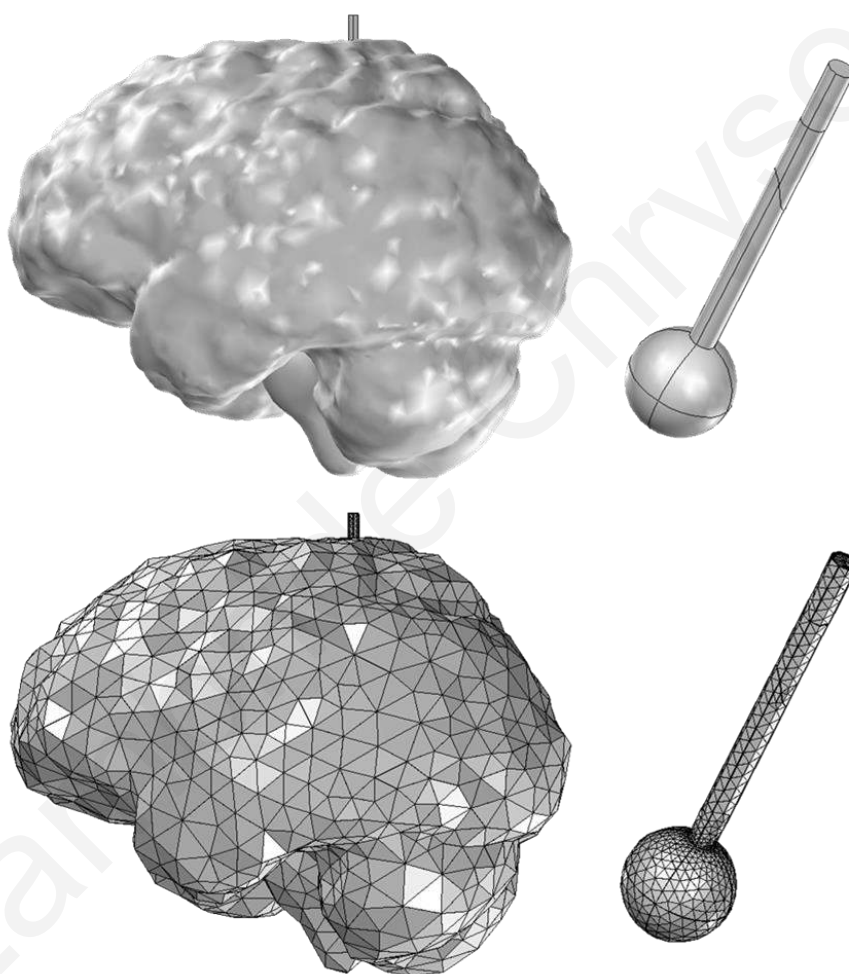
Figure 2.2: Three-dimensional finite elements model of the convection-enhanced delivery for brain cancer. Entire model consisted of 87,652 FEs (mainly, 67,540 tetrahedral FEs and 19,872 prismatic FEs).

2.2 <u>Mathematical model</u>

Following the modelling approach of Linninger *et al.* [24], the predictions of the drug distribution and pharmacokinetics are based on the conservation principles equations of mass, momentum and diluted species transport. The brain tissue is considered a porous medium. In this study, flow physics and mass transfer equations predict the interstitial fluid pressure (IFP), interstitial fluid velocity (IFV), and the distribution of therapeutic agents as a function of the pathophysiological parameters of the brain tumor as well as the drug size. Typically, in a CED administration, drugs are diluted in aqueous solution and are injected into the porous brain tumor tissue *via* an infusion catheter. The infusion motion of the diluted drug in the water is described by the mass and momentum conservation for an incompressible Newtonian fluid. Subsequently, the drug is distributed in the porous tissue according to the species transport equations [24].

2.2.1 *Conservation principle equations inside the catheter*

As mentioned above, the therapeutic agent is diluted in an aqueous solution at room temperature and this solution is considered incompressible Newtonian fluid. Thus, the viscous fluid motion of diluted drug solution in the catheter can be described using Navier-Stokes equation, neglecting inertial term (Stokes flow) due to slow fluid velocities and small catheter diameter (Reynolds number (Re) << 1). The mass and momentum conservation equations inside the catheter are determined, respectively, by [24]:

$$\rho \nabla \cdot \boldsymbol{u} = 0 \qquad \text{Equation 3}$$

$$\rho \frac{\partial u}{\partial t} = -\nabla p + \mu \nabla^2 \boldsymbol{u} \qquad \text{Equation 4}$$

where ρ is the water density, μ water viscosity at 298 K, $\boldsymbol{u}$ represents the fluid velocity, and p is the fluid pressure.

The drug transport in the catheter is established by the diluted species transport equation. This transportation is governed by both diffusion and convection. The species transport equation inside the catheter is defined by Equation 5.

$$\frac{\partial C_i}{\partial t} + \nabla \cdot (-D\nabla C_i + \boldsymbol{u} C_i) = 0 \qquad \text{Equation 5}$$

$$D = \frac{K_b T}{6 \pi \mu r_s} \qquad \text{Equation 6}$$

where C_i is the interstitial space concentration of drug, which is a dimensionless quantity, *i.e.*, the ratio of the drug concentration to the value of the concentration entering the catheter. *D* represents the diffusion coefficient of the drug in the aqueous solution and can be calculated using the Stokes−Einstein relationship, Equation 6. Generally, *D* is the diffusivity of a particle with radius r_s in dilute bulk solution with solvent viscosity *μ*, where K_b is the Boltzmann constant, and *T* is the temperature of the solution [32].

2.2.2 Conservation principle equations in the porous brain tissue

Infusate flow in the porous brain tissue obeys to the continuity equation and the extended Darcy's law [33]. The continuity equation of tumor fluid phase is given by Equation 7. The source term Q_m in Equation 7 represents the fluid exchanged between the tissue and the vascular system, and it is modelled using Starling's approximation [34, 35]:

$$\nabla \cdot \boldsymbol{u} = Q_m \qquad \text{Equation 7}$$

$$Q_m = L_p S_v (p_v - p_i) - L_{pl} S_{vl} (p_i - p_l) \qquad \text{Equation 8}$$

where $\boldsymbol{u}$ is interstitial fluid velocity (IFV), Q_m is fluid flux, L_p, S_v and p_v are the hydraulic conductivity of the vessel wall, vascular density and vascular pressure of the blood vessels respectively, whereas L_{pl}, S_{vl} and p_l are the corresponding quantities for the lymphatic vessels, and p_i is the interstitial fluid pressure (IFP).

The first term in Equation 8 refers to the fluid flux entering the tumor or the surrounding normal tissue from the blood vessels, while the second term refers to the fluid flux exiting through lymphatic system. It is important to note that the second term is zeroed in tumor tissue due to the dysfunctional lymphatic system [1].

It is necessary to introduce extended Darcy's law equations due to the presence of infusate flow from the CED catheter, to describe the fluid motion in porous tissues of the brain [24, 33]. The Brinkman equations extend Darcy's law to describe the dissipation of the kinetic energy by viscous shear, similar to the Navier-Stokes equations. Therefore, they are well appropriate for modeling fast flow in porous media, including transitions between fast flow in channels described by the Navier-Stokes

equations and slow flow in porous media governed by Darcy's law [36]. Thus, the momentum balance is given by Equation 9, where ε_p is the tissue porosity and k is the hydraulic conductivity of the interstitial space.

$$\rho \frac{\partial u}{\partial t} = \nabla \cdot \left[-p_i \boldsymbol{I} + \mu \frac{1}{\varepsilon_p} (\nabla \boldsymbol{u} + (\nabla \boldsymbol{u})^T) - \frac{2}{3}\mu \frac{1}{\varepsilon_p}(\nabla \cdot \boldsymbol{u})\boldsymbol{I} \right] - \left(k^{-1} + \frac{Q_m}{\varepsilon_p^2} \right)\boldsymbol{u}$$ Equation 9

Regarding the drug concentration distribution in the porous brain tissue, the diluted species transport equation, Equation 10, is applied, incorporating the exchange of drug between tissue and the blood vessels with the term Q [34, 35]. As discussed above, the total net transvascular drug flow equation, Equation 1, converts to Equation 11 by neglecting the oncotic pressure difference across the wall [1, 34, 35].

$$\frac{\partial C_i}{\partial t} + \nabla \cdot (-D_i \nabla C_i + \boldsymbol{u} C_i) = Q$$ Equation 10

$$Q = PS_v(C_v - C_i) + L_p S_v (1 - \sigma_f)[(p_v - p_i)]C_v$$ Equation 11

where D_i is the diffusion coefficient of the drug in the interstitial space, P is the vascular permeability of the drug, C_v is the vascular concentration of the drug, and σ_f is the reflection coefficient. Appling CED, the therapeutic agents are injected directly inside the interstitial space of tumor tissue, thereby the vascular drug concentration (C_v) is considered negligible compared to the interstitial space drug concentration (C_i). Thus, the value of C_v is zero.

In this study, the therapeutic agent is considered as spherical neutral molecule and the vessel wall openings are modeled as cylinder pores [32]. To investigate the direct effect of the vascular wall pore and drug sizes on the drug concentration distribution, the theory for hindered transport of rigid solutes through liquid filled porous is introduced. Using this theory, the hydraulic conductivity of microvascular walls (L_p) and the drug vascular permeability (P) are explicitly estimated based on the above parameters. The hydraulic conductivity of vessel walls is calculated using Equation 12. Also, the vascular permeability of the drug and the reflection coefficient are defined by Equation 13 and Equation 14, respectively [32, 34, 35].

$$L_p = \frac{\gamma r_0^2}{8\mu L_{vw}}$$ Equation 12

$$P = \frac{\gamma H D}{L_{vw}}$$ Equation 13

$$\sigma_f = 1 - W$$ Equation 14

where γ is the fraction of vessel all surface area occupied by pores, r_o is the pore radius, μ is the viscosity of plasma at 310 K, and L_{vw} is the thickness of the vessel wall. D is the diffusion coefficient of a particle, given by the Stokes-Einstein relationship, Equation 6, where μ is the plasma viscosity. H and W are hydrodynamic coefficients for neutral spheres in cylindrical pores, and can be calculated by [34, 35]:

$$H = \frac{6\pi F}{K_t}$$

Equation 15

$$W = \frac{F(2-F)K_s}{2K_t}$$

Equation 16

where F is the partition coefficient, $F = (1-\lambda)^2$, λ is the ratio of the drug size to the vessel wall pore size. The coefficients K_t and K_s are determined by Equation 17, where a and b are constant coefficients, Table 1 in Annex I [34, 35].

$$\binom{K_t}{K_s} = \frac{9}{4}\pi^2\sqrt{2}(1-\lambda)^{-5/2} + \left[1 + \sum_{n=1}^{2}\binom{a_n}{b_n}(1-\lambda)^n\right] + \sum_{n=0}^{4}\binom{a_{n+3}}{b_{n+3}}\lambda^n$$

Equation 17

2.2.3 Values of model parameters and boundary conditions

For a realistic 3D FE model, data from experimental studies are used to determine the biomechanical properties. As in pertinent studies, the diameters of vascular wall pores are set to 50, 100 and 150nm [37, 38], whereas the the hydraulic conductivity of the tumor interstitial space, k, is taken equal to 7.5×10^{-14} and 7.5×10^{-13} $m^2(Pa\ s)^{-1}$ [3]. Brain cancer studies suggest that the optimal size of nanoparticles ranges from 20 to 70 nm in diameter to easily diffuse into tumor ECM [7, 18]. Thus, the diameters of therapeutic agents are adjusted to 1, 20, 60nm in order to investigate the impact of a wide range of sizes. Summarizing, all values of physiological properties are shown in Table 2 in Annex I.

For each geometry domain, the aforementioned conservation principles equations of mass and momentum as well as the diluted species transport equations of the CED biomechanical model are discretized and solved numerically together using the commercial FE software COMSOL Multiphysics 5.5 (COMSOL Inc., Burlington, MA, USA). The Brinkman Equations interface of the FE software is used, providing the conservation of mass and momentum equations that can fully describe the fluid dynamics within each geometry domains. The Brinkman Equations interface computes both the velocity filed and pressure which are the dependent variables. Additionally,

both the velocity (vector) field and pressure (scalar) are discretized using linear Lagrange basis functions. Likewise, the drug concentration (scalar) is discretized using linear Lagrange basis functions. Moreover, the domain of analysis is meshed using FEs, as illustrated in Figure 2.2.

According to clinical CED studies [9, 39-41], infusion flow rate, Q_f, is a wide range from 0.025 to 0.75mL/h and the infusion volume is fluctuated between 0.25 and 185mL. A flow rate of 0.5mL/h and an infusion volume of 3mL are selected for the simulations. Therefore, at the inlet surface, A, of the catheter, the normal inlet velocity (*i.e.,* $U_o=Q_f/A$) is taken equal to 2.2×10^{-5} m/s for 6 hours. This is the duration of drug injection into the tumor tissue. Also, at this surface, the drug concertation is set to unit for the same period. The normal stresses on the outer brain surfaces is equal to a zero reference pressure (*i.e.*, $\boldsymbol{n}\cdot\boldsymbol{\sigma} = \boldsymbol{0}$, where $\boldsymbol{n}$ corresponds to the outward unit normal vector to the surface of the 3D model). At the catheter interfaces, a no-slip boundary condition is applied for fluid velocity (*i.e.*, $\boldsymbol{u}=\boldsymbol{0}$) and additionally, a zero-flux boundary condition is set for the transport of diluted species (*i.e.*, $\boldsymbol{n}\cdot(D\nabla C_i+\boldsymbol{u}C_i)=0$). The latter boundary condition is also set at the outer brain surfaces. Regarding initial value, both the fluid velocity and pressure variables are set to zero for all geometry domains. In contrast, the initial value of the drug concentration is zero in the entire geometry except for the catheter domain, where the initial value is unit.
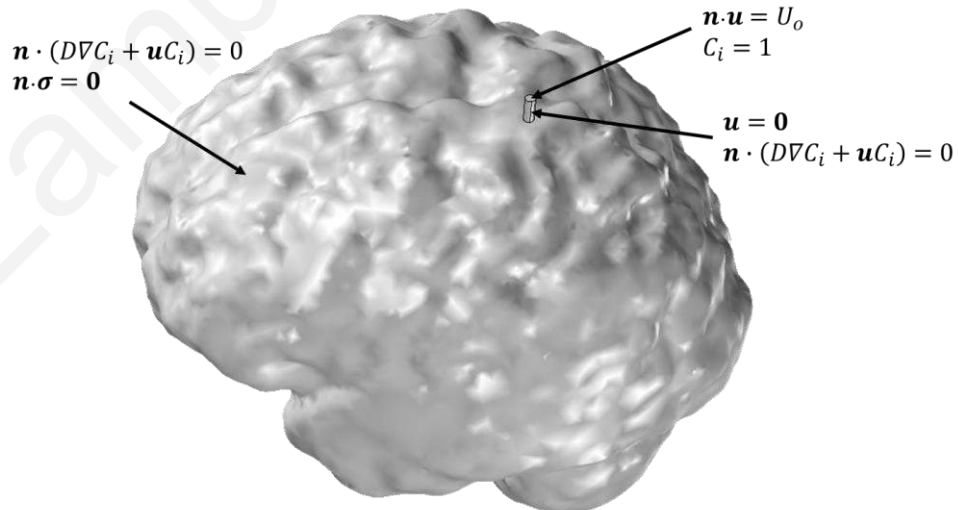
Figure 2.3: Computational boundary conditions of the 3D model.

Chapter 3

3 RESULTS AND DISCUSSION

As part of this thesis, a series of simulations have been performed to fully comprehend the fluid dynamics and the distribution of the drug concentration as a function of the pathophysiological parameters of the tumor tissue and the drug sizes. Initially, for a given low hydraulic conductivity of the tumor interstitial space value, k, and different drug sizes, D_s, the effect of the vascular wall pore size of tumor tissue, D_o, is extensively investigated. As a next stage, the tumor interstitial space hydraulic conductivity increases in order to obtain a complete picture of the fluid behavior and the therapeutic agent concentration for the physiological properties of the tumor. Finally, the heterogeneity of the drug distribution is examined for all pathophysiological conditions. The visualization of the results focuses on the tumor tissue. It is important to note that the infusion parameters of CED are constant for all simulations.

3.1 IFP and IFV profiles in tumor tissue

As discussed above, the diameters of the vessel wall pores are selected to be 50, 100 and 150 nm. Obviously, the size of the drug does not influence the fluid dynamics, since the calculation of pressure and velocity is achieved by solving conservation of mass and momentum together. On the other hand, the hydraulic conductivity of the vascular wall depends proportionally on the size of the openings present in the vascular wall, Equation 12. Therefore, the fluid flow and pressure are influenced. As the infusion duration is 6 hours, the interstitial fluid pressure (IFP) and interstitial fluid velocity (IFV) of the tumor tissue are studied during and after infusion flow. Their spatial profiles remain constant until the infusion stops and other steady-state behaviors are achieved. Tumor IFP and IFV are significantly affected by changing the pathophysiological parameter of the tumor tissue, especially when the impact of the infusion flow is eliminated.

3.1.1 Effect of vascular wall pore size when using the lowest value of interstitial space hydraulic conductivity

In order to study the impact of vascular wall pore size, the hydraulic conductivity of tumor interstitial space is initially taken equal to 7.5×10^{-14} m^2(Pa s)$^{-1}$for the following set of simulations. Firstly, the case of pores with a diameter of 50 nm is examined. Figure 3.1A illustrates a sagittal view in the center of the tumor tissue, showing both the spatial distribution of IFP and IFV during CED, for the pore diameter of 50nm. The interstitial infusion of the therapeutic agent by a catheter creates a pressure gradient, permitting enhanced distribution of the brain tumor. A high pressure gradient occurs, causing high interstitial fluid velocities. The maximum pressure and velocity are 312.8 kPa and 22.6 μm/s, respectively, at the catheter outlet surface. After the injection, Figure 3.2A, the interstitial fluid pressure is evenly distributed with a maximum value of 1.9 kPa at the center of the tumor tissue. The IFP decreases radially outward, reaching that of normal tissue at the boundary of the tumor. In contrast, the interstitial fluid velocity has the reverse distribution from IFP, as it increases and reaches a maximum value of 0.14 μm/s at the margin of the tumor.

Additionally, the pore diameter of the vascular walls changes to 100 nm and 150 nm. These modifications affect insignificantly the IFP and IFV distributions during CED, as shown in Figure 3.1B and C. This indication is also illustrated in Figure 3.3B, which presents the IFP and IFV as function of the relative distance from tumor center during infusion for each pore diameter. In all cases of pore diameters, IFP decreases with distance from the center of the tumor in the same way. However, after 6 hours, the IFP and IFV spatial distributions are affected by increasing the diameter of the pores, Figure 3.2. When the pore diameter is 100 nm, the interstitial fluid pressure at the center of tumor is 2 kPa which is equal to the micro-vascular pressure of the blood vessels. This pressure value remains constant up to 0.5 relevant distance from the tumor center. Likewise, in the case of 150 nm pore diameter, IFP is equal to the micro-vascular pressure of the blood vessels expect in a thin shell near the boundary, Figure 3.3B. Regarding IFV profiles, Figure 3.3C, the maximum velocity at the tumor margin increases with the pore diameter of vascular wall. For 100 and 150 nm pore diameters, the maximum values of interstitial fluid velocity are 0.30 and 0.45 μm/s at the tumor margin, respectively.

Figure 3.1: FE simulation results during CED. A sagittal view in the center of the tumor tissue showing both the spatial distribution of interstitial fluid pressure, IFP, (in kPa) and interstitial fluid velocity, IFV, (in μm/s) during CED, for 7.5×10^{-14} m^2(Pa s)$^{-1}$ hydraulic conductivity of the tumor interstitial space and for different diameters of vascular wall pores: (**A**) 50 nm, (**B**) 100 nm, and (**C**) 150 nm.

Figure 3.2: FE simulation results after CED. A sagittal view in the center of the tumor tissue showing both the spatial distribution of interstitial fluid pressure, IFP, (in kPa) and interstitial fluid velocity, IFV, (in μm/s) after CED, for 7.5×10^{-14} m^2(Pa s)$^{-1}$ hydraulic conductivity of the tumor interstitial space and for different diameters of vascular wall pores: (**A**) 50 nm, (**B**) 100 nm, and (**C**) 150 nm.

Figure 3.3: Plots of IFP and IFV as a function of relevant distance from the tumor center for different diameters of vascular wall pores and 7.5×10^{-14} m^2(Pa s)$^{-1}$ hydraulic conductivity of the tumor interstitial space. **(A)** A sagittal view in the center of the tumor tissue where the IFP and IFV graphs were created along the red line. *In silico* predicted fluid pressure and magnitude velocity of the tumor interstitial space: **(B)** during and **(C-D)** after CED.

3.1.2 Effect of vascular wall pore size when using the highest value of interstitial space hydraulic conductivity

Further step of this study is to investigate the effect of the hydraulic conductivity of the tumor interstitial space. Thus, the following simulation is carried out using a greater hydraulic conductivity value, 7.5×10^{-13} m^2(Pa s)$^{-1}$. In the case of 50 nm diameter pore of vascular wall, the maximum interstitial space pressure and velocity are 31.4 kPa and 22.6 μm/s, respectively, at the catheter outlet surface, Figure 3.4A. When the infusion flow stops, the interstitial fluid pressure is consistently distributed with a maximum value of 0.7 kPa at the center of the tumor tissue. The interstitial fluid velocity increases, reaching a maximum value of 0.26 μm/s at the margin of the tumor, Figure 3.5A.

Moreover, the simulations are performed with diameters of 100 and 150 nm. During the infusion flow, the IFP profiles are slightly shifted to higher values with when the diameters of the vascular wall pores are increased. Therefore, the IFV values at the tumor margin rise due to the higher pressure gradient, Figure 3.4B and C. This indication is also demonstrated in the IFP plots as a function of relevant distance from the center, Figure 3.6B. After the injection, the IFP and IFV distributions change considerable, Figure 3.5B and C. It is observed that these profiles are more sensitive to the pore diameter variation for the higher value of the tumor tissue hydraulic conductivity. Both the IFP value in the tumor center and the IFV value at the tumor margin rise with the diameter of vascular wall pores. In case of the 100 nm pore diameter, the tumor center IFP is doubled relative to that of 50 nm pore diameter, and for 150nm the corresponding value reaches 1.9kPa, Figure 3.6C. Furthermore, the maximum value of IFV is obtained at tumor margin for 150 nm pore diameter and it is equal to 1.28 μm/s, Figure 3.6D.
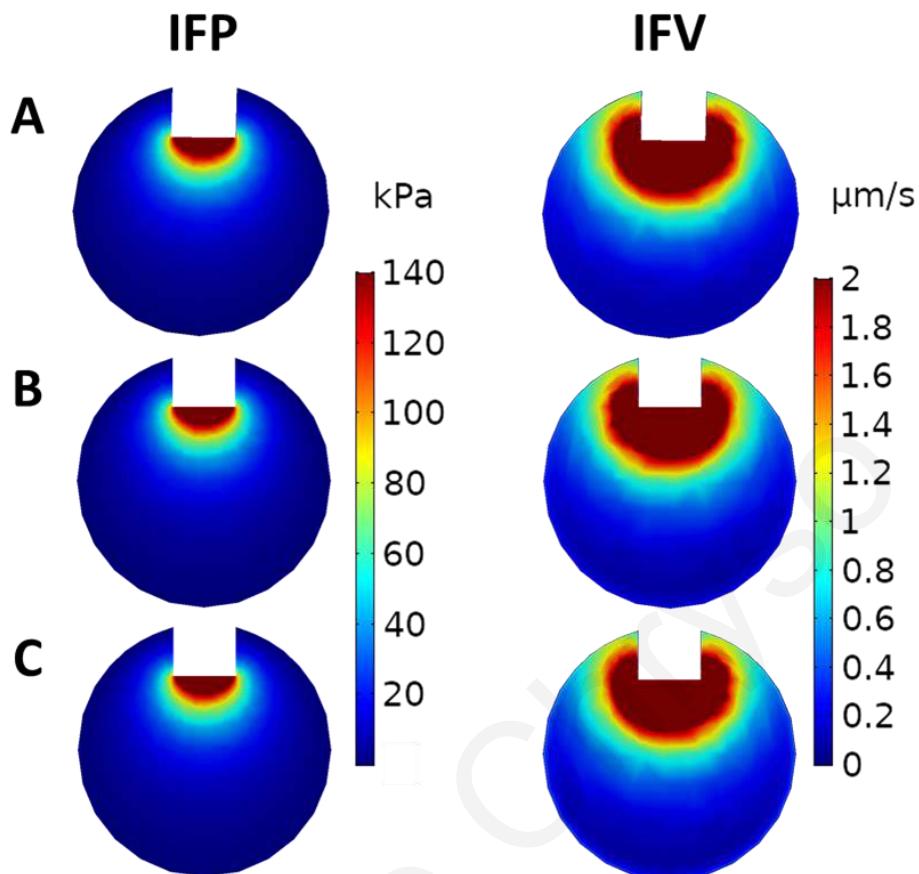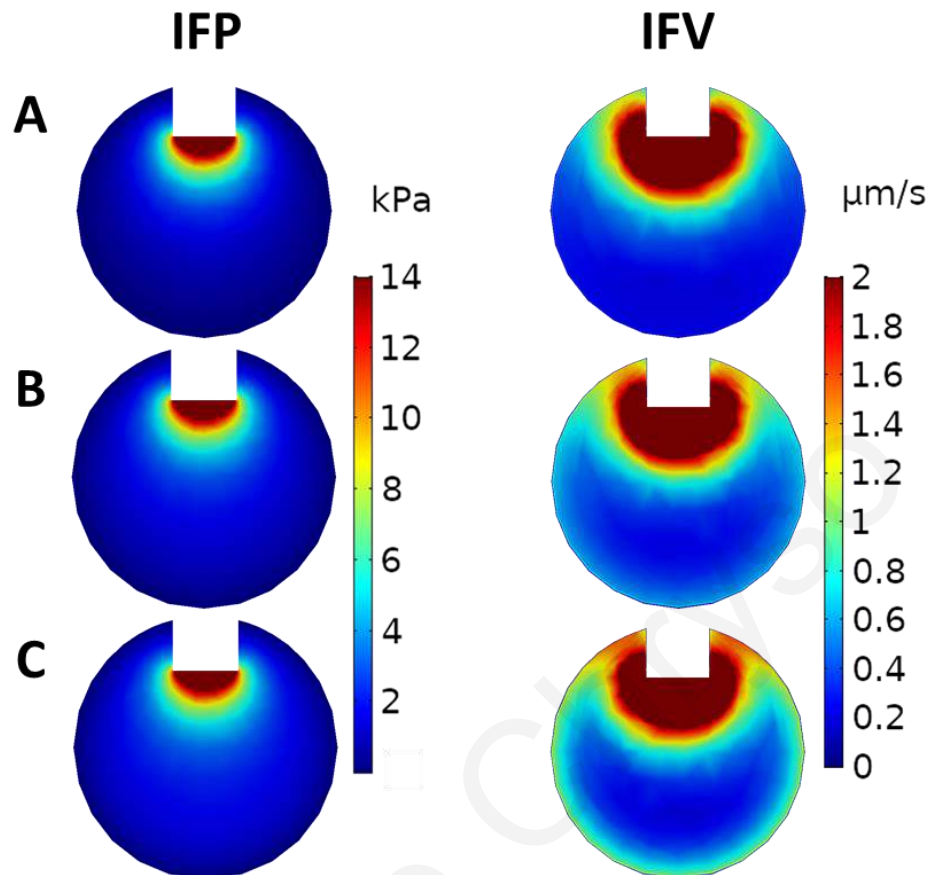
Figure 3.4: FE simulation results during CED. A sagittal view in the center of the tumor tissue showing both the spatial distribution of interstitial fluid pressure, IFP, (in kPa) and interstitial fluid velocity, IFV, (in μm/s) during CED, for 7.5×10^{-13} m^2(Pa s)$^{-1}$ hydraulic conductivity of the tumor interstitial space and for different diameters of vascular wall pores: (**A**) 50 nm, (**B**) 100 nm, and (**C**) 150 nm.
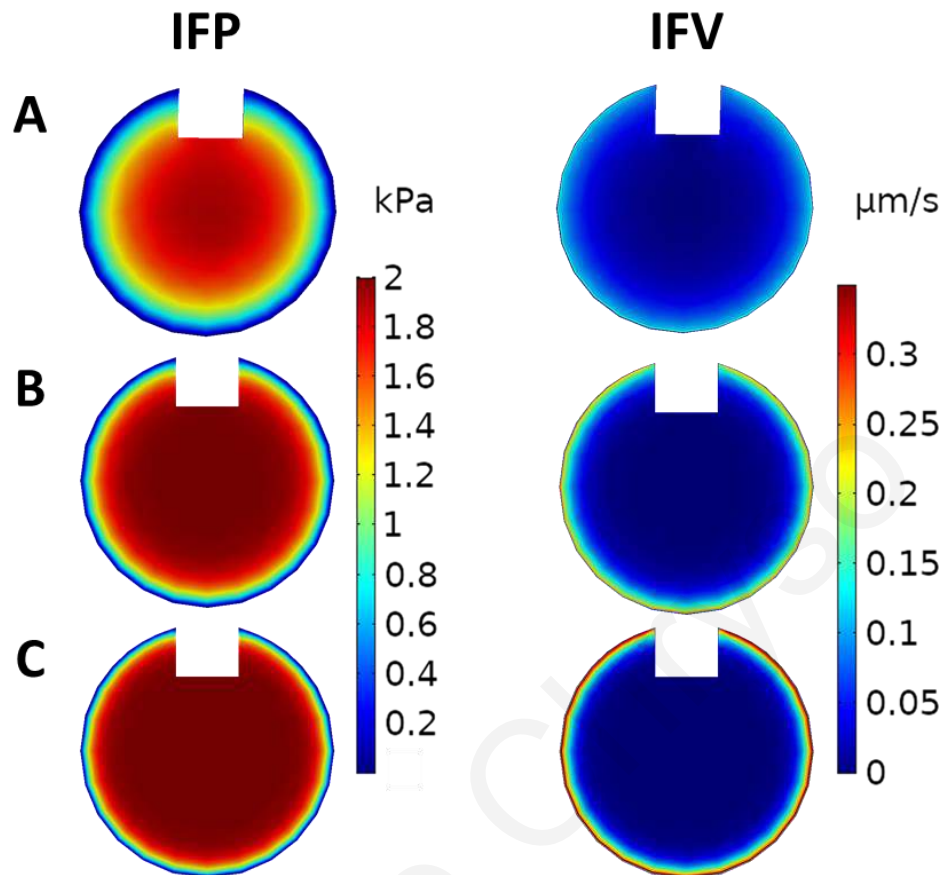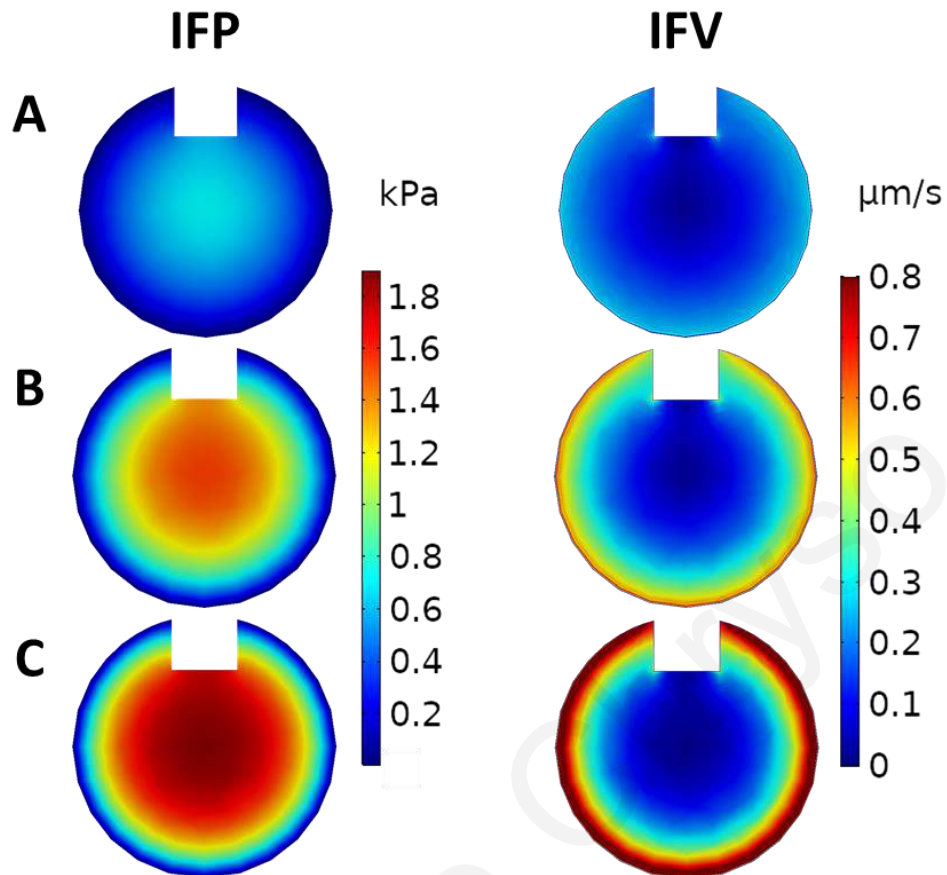
Figure 3.5: FE simulation results after CED. A sagittal view in the center of the tumor tissue showing both the spatial distribution of interstitial fluid pressure, IFP, (in kPa) and interstitial fluid velocity, IFV, (in μm/s) after CED, for 7.5×10^{-13} m^2(Pa s)$^{-1}$ hydraulic conductivity of the tumor interstitial space and for different diameters of vascular wall pores: (**A**) 50 nm, (**B**) 100 nm, and (**C**) 150 nm.
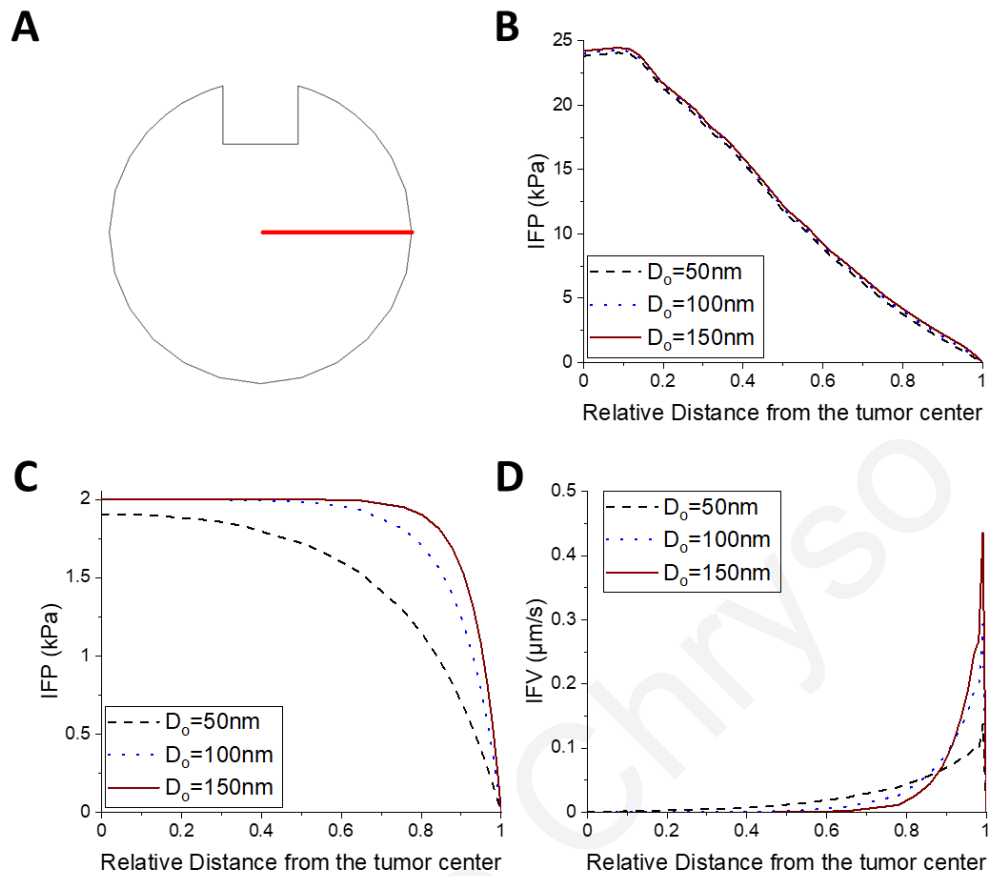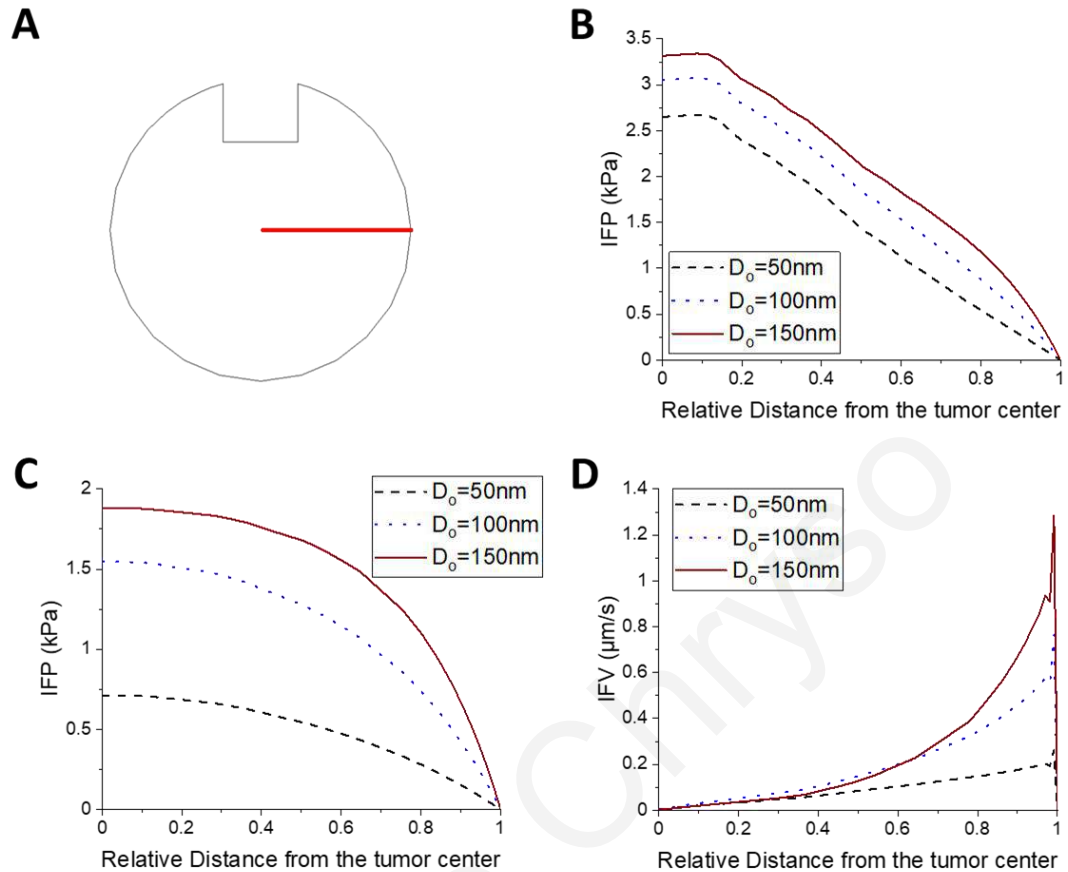
Figure 3.6: Plots of IFP and IFV as a function of relevant distance from the tumor center for different diameters of vascular wall pores and 7.5×10^{-13} $m^2(Pa\ s)^{-1}$ hydraulic conductivity of the tumor interstitial space. **(A)** A sagittal view in the center of the tumor tissue where the IFP and IFV graphs were created along the red line. *In silico* predicted fluid pressure and magnitude velocity of the tumor interstitial space: **(B)** during and **(C-D)** after CED.

Comparing the above results, the IFP and IFV distributions are significantly influenced, changing the pore diameters and tissue hydraulic conductivity values. It is worth noting that the impact of pore sizes on IFP and IFV profiles is more considerable when using the highest value of tissue hydraulic conductivity. Specifically, for the lowest value of the tissue hydraulic conductivity, the pore diameter modifications insignificantly affect the IFP and IFV profiles, during CED. In addition, by increasing the tissue hydraulic conductivity values by an order of magnitude, the maximum IFP values decrease by the same order of magnitude during the infusion flow. Besides, after infusion, the reduction in the pore size of vascular walls results in the decrease of the hydraulic conductivity of tumor vessels, *Lp,* and the tumor IFP. It is remarkable that when the diameter of the pores decreases, the velocity within the tumor is higher, whereas flow from the boundary is lower.

3.2 <u>D r u g   c o n c e n t r a t i o n   d i s t r i b u t i o n</u>

To extensively investigate the drug distribution, a range of drug physicochemical and microenvironments properties have been considered. It is well known that the transport mechanism of therapeutic agents can be either through diffusion or convection. The convection transport is owing to pressure gradients, thus the IFP and IFV profiles are vital for the drug delivery. The therapeutic agents of 1, 20 and 60 nm in diameter are selected. By increasing the drug size, the diffusion coefficient of the drug through the tumor interstitial space decreases and it can be estimated experimentally [42]. It is important to note that the relative size of the drug to the vessel wall pore size determines the permeability of the drug across the vessels, using Equation 13, Equation 15 and Equation 17. The following simulations are performed for the aforementioned values of the vascular wall pore diameter and hydraulic conductivity of the tumor interstitial space.

The drug is injected in the tumor tissue with a catheter outer diameter 3 mm and infusion flow 0.5 ml/h. The duration under study is 48 hours where the infusion period is 6 hours. The concentration is a dimensionless quantity defined by the ratio of the local drug concentration to the drug concentration that enters from the catheter. Hence, the relative concentration of drug is unit at catheter inlet.

3.2.1 *Effect of vascular wall pore size when using the lowest value of interstitial space hydraulic conductivity*

Initially, the hydraulic conductivity of the tumor interstitial space is equal to 7.5×10^{-14} m^2(Pa s)$^{-1}$ and the diameter of vessel wall pore is set to 50 nm. Figure 3.7 illustrates a sagittal view in the center of the tumor tissue, presenting the spatial distribution of different drug sizes in three snapshots, *i.e.*, 6 hours, 12 hours and 24 hours. All spatial drug distributions are symmetric in vertical axis. In case of the 1nm drug diameter, the highest drug concentration is located near the infusion site. These nanoparticles have a high diffuse coefficient in the tissue due to their small size. As the relative size of the drug to the vessel wall pore size is large, the vascular permeability is very high, enhancing the diffusion through the pores. Hence, a significant drug amount can be lost because the nanoparticles can easily pass into the blood vessel due to concentration gradient. Figure 3.7A demonstrates the spatial distribution of the 1nm drug over the time. When the infusion stops, the average relative concentration of

therapeutic agent reaches 0.36 in tumor tissue, and then decreases sharply to zero, Figure 3.8.

Figure 3.7: FE simulation results. A sagittal view in the center of the tumor tissue showing the spatial distribution of drug concentration for 7.5×10^{-14} m^2(Pa s)$^{-1}$ hydraulic conductivity of the tumor interstitial space, 50 nm diameter of vascular wall pores, and for different diameters of the therapeutic agent: (**A**) 1 nm, (**B**) 20 nm, and (**C**) 60 nm (columns) in three snapshot: 6hrs, 12hrs and 24hrs (rows).

The therapeutic agents with 20 nm diameter have lower values of vascular permeability and thereby, the extravascular drug transport is reduced. This type of nanoparticle is able to penetrate, covering almost the entire tumor region during CED administration. The maximum average relative concentration of drug in tumor tissue is 0.94 at 6 hours, Figure 3.8. After the infusion, the average concertation decreases and the maximum drug concentration is located both in the center of tumor tissue and near the catheter outlet. It is observed that the drug concentration decreases radially outward while in a thin shell near the boundary, there is significant amount of drug, Figure 3.7B. The elevation in drug concentration at the tumor margin is due to the sharply decrease of fluid velocity in the tumor periphery. Typically, the drug can be transport either through diffusion or convection in the interstitial tumor space. However, at the tumor

margin the fluid velocity reaches the maximum value and suddenly decreases to zero due to the absence of pressure gradients in the peripheral region of the tumor. Hence, the only way for the drug to escape from the tumor margin is the transportation through diffusion. One day after the procedure has been started, the local drug concentration is 0.6 near the outlet surface of catheter, and 0.55 in the center of tumor tissue, while the average relative drug concentration is 0.19.

When 50 nm diameter of vessel wall pores is investigated, the nanoparticles with 60 nm diameter cannot cross the pores. They can transport through diffusion into the interstitial space of tumor with lower diffusion coefficient compared to the other two drug sizes *i.e.,* 1 nm and 20 nm. Similarly to 20nm drug size, the drug of 60 nm diameter is distributed in a large volume of tumor tissue during infusion flow, Figure 3.7C. The maximum average relative concentration in tumor tissue is equal to 0.97 at 6 hours. Additionally, after 6 hours, the drug is dispersed in the same way with the 20 nm drug size. The average relative concentration of drug is higher during the whole period, Figure 3.8. After a day, the average relative drug concentration is 0.23.

Figure 3.8: Plots of the average relative concentration in tumor tissue as a function of time for different diameters of therapeutic agents and 7.5×10^{-14} m^2(Pa s)$^{-1}$ hydraulic conductivity of the tumor interstitial space and 50 nm diameter of vascular wall pores.

The following set of simulations is carried out in order to investigate the effect of pore diameter of tumor vessel walls on the drug concentration and spatial distribution. To achieve this, the pore diameter changes from 50 to 100 nm and the hydraulic

conductivity of tumor interstitial space remains at 7.5×10^{-14} $m^2(Pa\ s)^{-1}$. This modification affects insignificantly the spatial distribution of drug with 1 nm diameter, Figure 3.9A. In the case of the 20 nm and 60 nm drug diameters, higher drug concentrations is observed in tumor center, Figure 3.9B and C. This is a result of the IFV profile, because when the diameter of the pores increases, the velocity within the tumor is lower, whereas flow at the boundary is higher. Therefore, the convection transport of drug is reduced within the tumor center, making diffusion the main transport mechanism. The convection contribution increases near the tumor boundary, where the drug concentration is low. For 20 and 60 nm drug diameter, the maximum average relative concentrations of drug are 0.9 and 0.95 at 6hrs, respectively, while the maximum average relative concentration values after a day are 0.17 and 0.29, respectively, Figure 3.10.
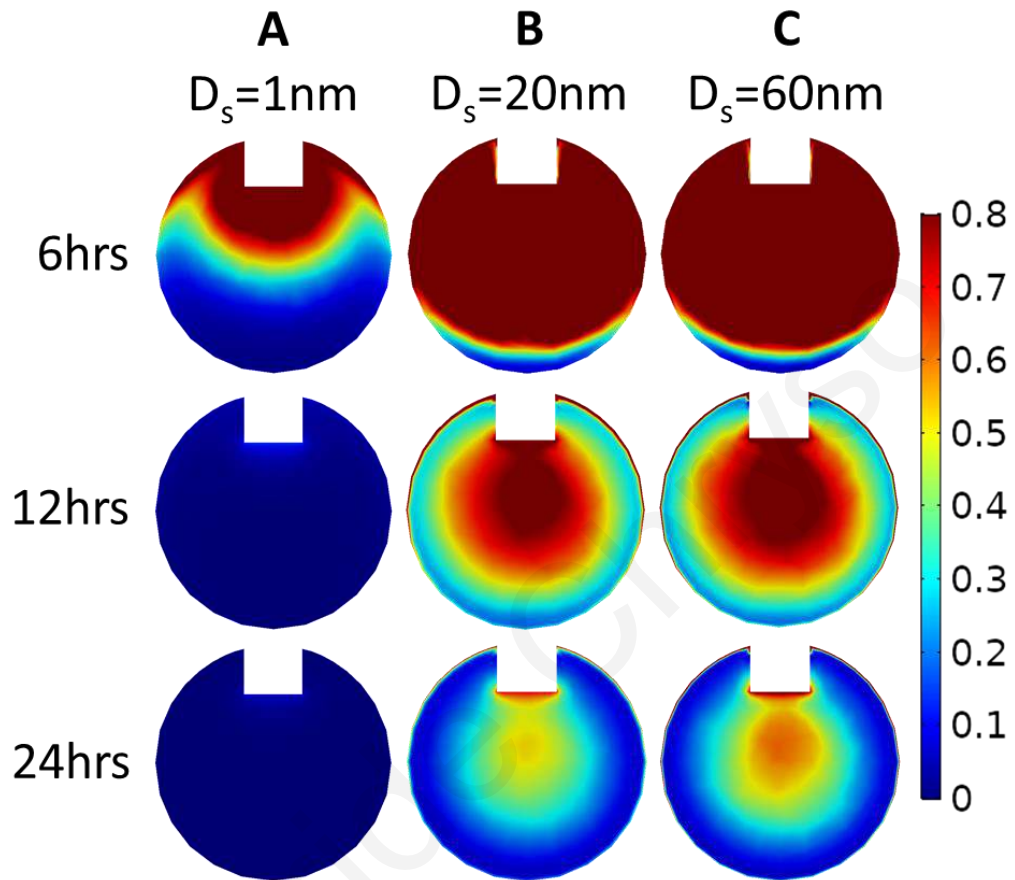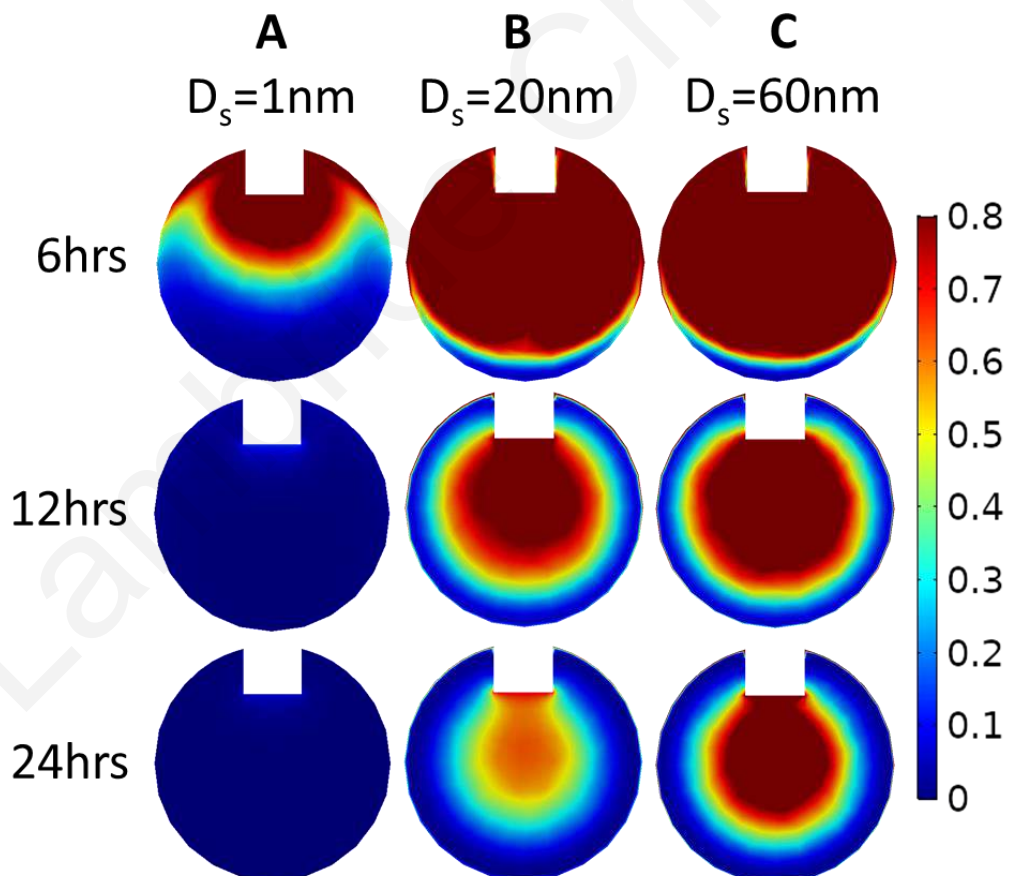

Figure 3.9: FE simulation results. A sagittal view in the center of the tumor tissue showing the spatial distribution of drug concentration for 7.5×10^{-14} $m^2(Pa\ s)^{-1}$ hydraulic conductivity of the tumor interstitial space, 100 nm diameter of vascular wall pores, and for different diameters of the therapeutic agent: (**A**) 1 nm, (**B**) 20 nm, and (**C**) 60 nm (columns) in three snapshot: 6hrs, 12hrs and 24hrs (rows).
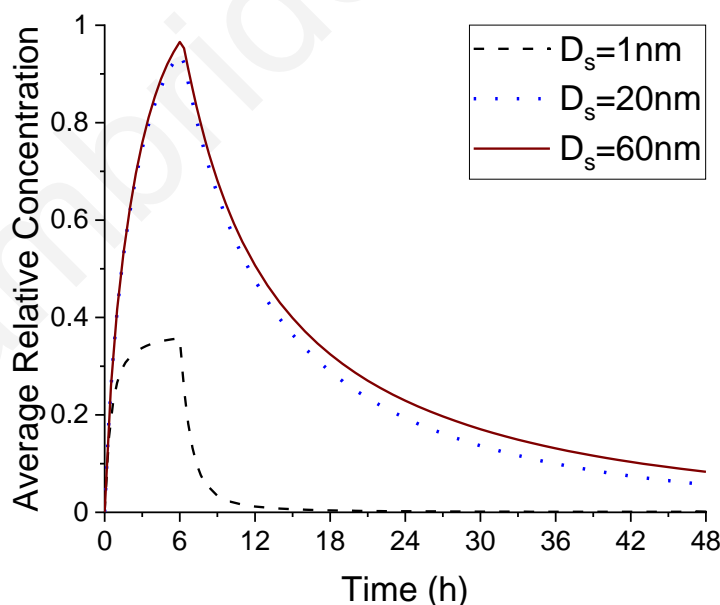
.
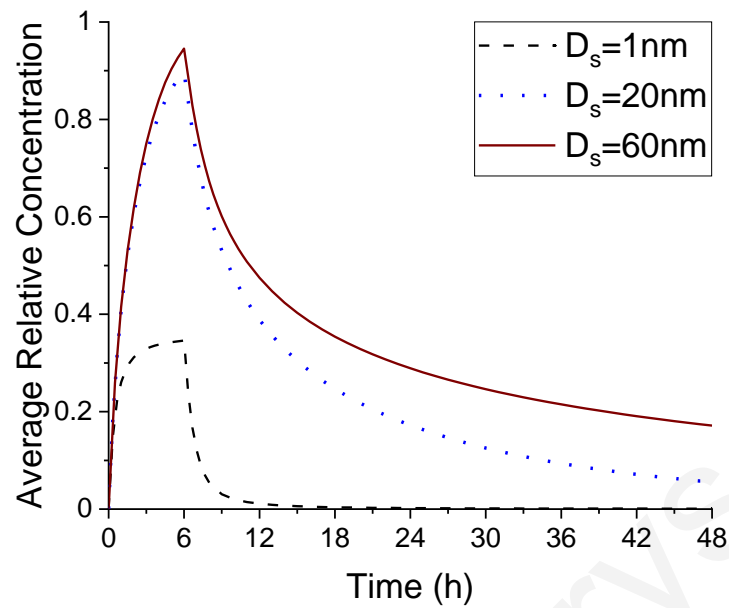
Figure 3.10: Plots of the average relative concentration in tumor tissue as a function of time for different diameters of therapeutic agents and 7.5×10^{-14} m^2(Pa s)$^{-1}$ hydraulic conductivity of the tumor interstitial space and 100 nm diameter of vascular wall pores.

Afterwards, the pore diameter of tumor vascular wall is set to 150 nm and the hydraulic conductivity of tumor interstitial space is unchanged. The nanoparticles with 1 nm diameter behave similarly with previous simulations, Figure 3.11A. The maximum average relative concentration of drug is 0.34 at 6 hours, Figure 3.12. Moreover, for 20 nm drug diameter, the drug concentration profile is identically with that of 100 nm pore diameter, Figure 3.11B. The most important results of this simulation set is the spatial distribution of the drug with 60 nm diameter. Further increase in pore diameter causes negligible convection transport within the tumor center. In addition, the drug losses from blood vessels are in low levels due to the low vascular permeability of the drug. The vascular permeability becomes important when the relative size of the drug to the vessel wall pore size is greater than 0.3. In this case, the relative size is 0.4 corresponding to the very low vascular permeability value. Therefore, the drug concentration in tumor center remains at high levels during a day, Figure 3.11C, with an average 0.35 relative drug concentration, Figure 3.12.

Figure 3.11: FE simulation results. A sagittal view in the center of the tumor tissue showing the spatial distribution of drug concentration for 7.5×10^{-14} $m^2(Pa\ s)^{-1}$ hydraulic conductivity of the tumor interstitial space, 150 nm diameter of vascular wall pores, and for different diameters of the therapeutic agent: (**A**) 1 nm, (**B**) 20 nm, and (**C**) 60 nm (columns) in three snapshot: 6hrs, 12hrs and 24hrs (rows).

Figure 3.12: Plots of the average relative concentration in tumor tissue as a function of time for different diameters of therapeutic agents and 7.5×10^{-14} $m^2(Pa\ s)^{-1}$ hydraulic conductivity of the tumor interstitial space and 150 nm diameter of vascular wall pores.

Consequently, these simulation sets show the effect of the pore diameter of tumor vascular wall for the lower value of interstitial space hydraulic conductivity. Plots in Figure 3.13 corresponded to each drug size, *i.e.*, 1 nm, 20 nm and 60 nm compering the average relative concentration of the drug for different diameters of vascular wall pore. It is observed that for 1nm and 20 nm drug size, the average relative concentration of drug is affected insignificantly by changing the diameter of vascular wall pore, as a function of time. However, for nanoparticles with 60 nm size and after 12 hours, the average relative concentration increases with the pore diameter of tumor vessels wall. This indication is promising for effective treatment of brain cancer.
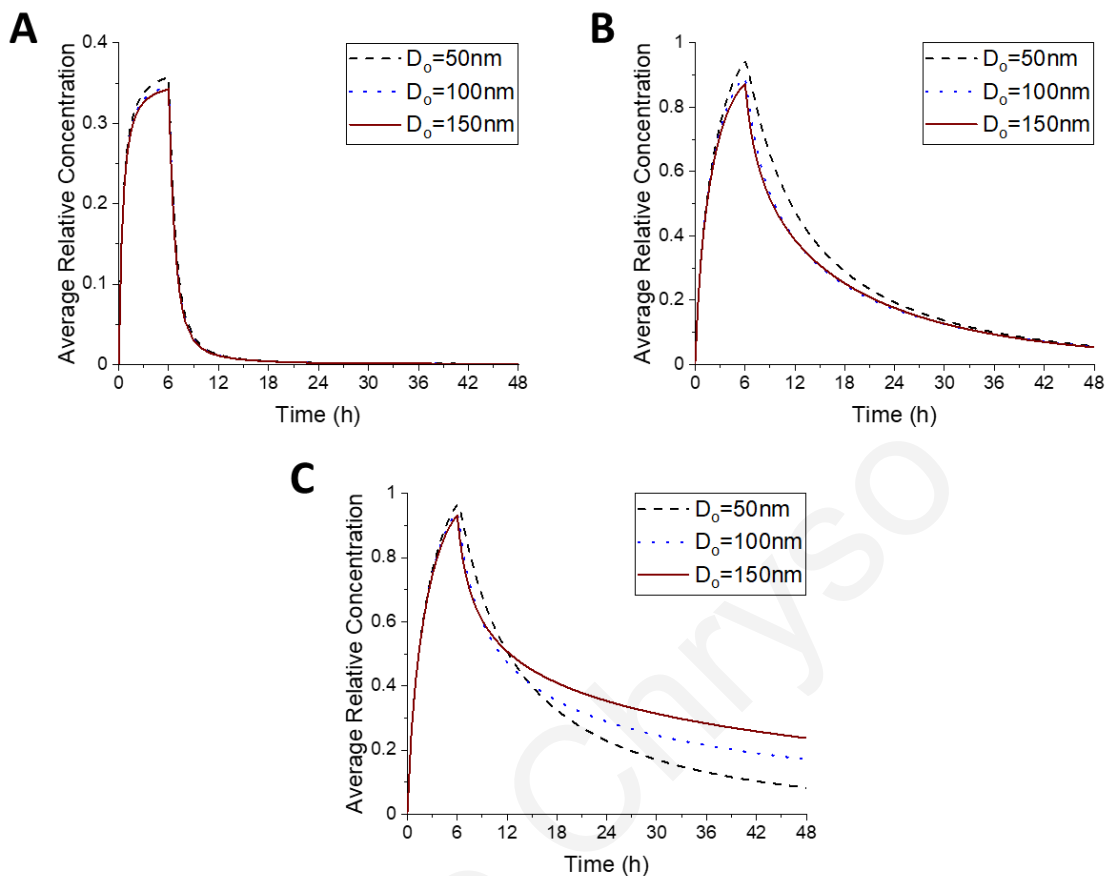
Figure 3.13: Plots of the average relative concentration in tumor tissue as a function of time for 7.5×10^{-14} $m^2(Pa\ s)^{-1}$ hydraulic conductivity of the tumor interstitial space and different diameters of vascular wall pores, and different diameters of the therapeutic agent: (**A**) 1 nm, (**B**) 20 nm, and (**C**) 60 nm.

3.2.2 Effect of vascular wall pore size when using the highest value of interstitial space hydraulic conductivity

As a next step of this project, to examine the effect of higher hydraulic conductivity of tumor interstitial space, the below simulations are performed for 7.5×10^{-13} m^2(Pa s)$^{-1}$ hydraulic conductivity. The diameter ranges of drug and vascular wall pore remain the same with the previous simulations. As mentioned, by increasing hydraulic conductivity of tumor tissue, the interstitial fluid pressure decreases and the interstitial fluid velocity rises within the center of tumor. Thus, the interstitial drug transport through convection is enhanced from the center to periphery, allowing the drug to escape easily from tumor tissue.

In case of the 50 nm pore diameter of vessel walls, Figure 3.14 depicts a sagittal view in the center of the tumor tissue, presenting the spatial distribution of different drug sizes in three snapshots, i.e., 6 hours, 9 hours and 12 hours. All spatial drug distributions are symmetric in vertical axis. For 1 nm drug size, the highest drug concentration is near the infusion site, Figure 3.14A. The average relative concentration reach the peak value of 0.35 at 6 hours and then drops dramatically to zero, Figure 3.15. However, the nanoparticles with 20 nm diameter are distributed similarly to those with 60 nm diameter, as shown Figure 3.14B and C. The drug concentration is higher at the tumor boundary, but the drug dispreads sufficiently within the tumor tissue. Additionally, the average relative concentrations of these drug sizes are identically over time, reaching 0.8 at 6 hours, Figure 3.15.
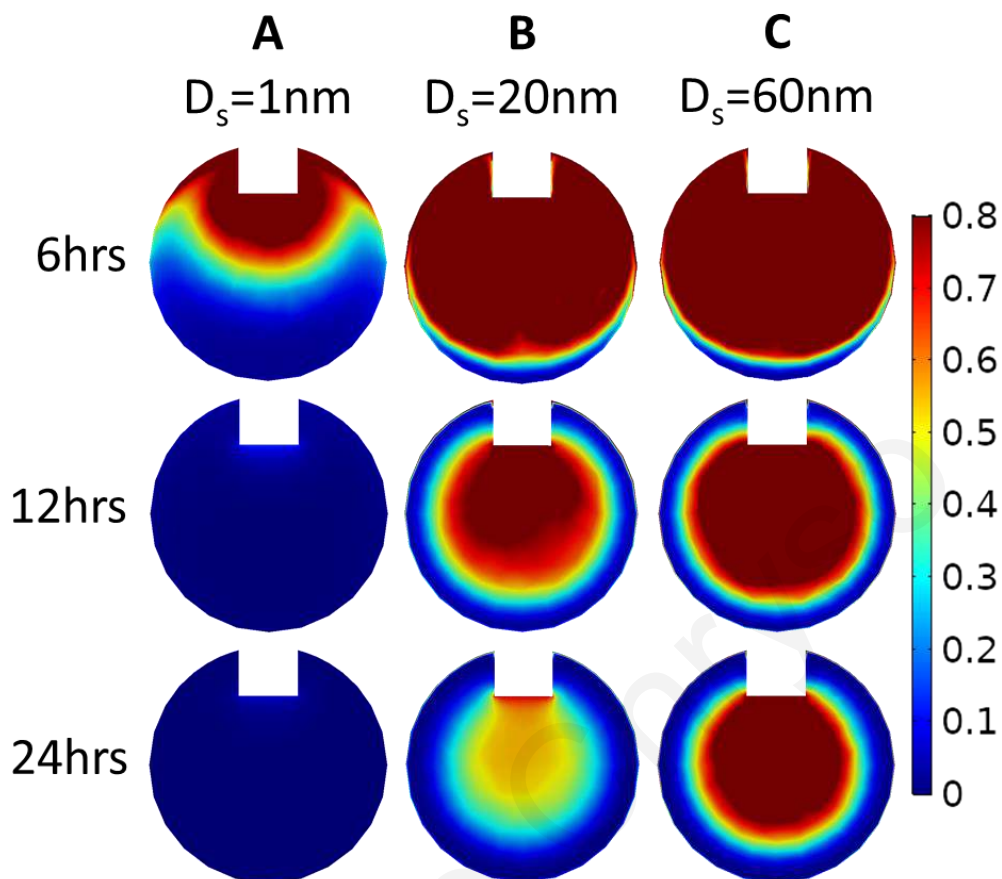
Figure 3.14: FE simulation results. A sagittal view in the center of the tumor tissue showing the spatial distribution of drug concentration for 7.5×10^{-13} m^2(Pa s)$^{-1}$ hydraulic conductivity of the tumor interstitial space, 50 nm diameter of vascular wall pores, and for different diameters of the therapeutic agent: (**A**) 1 nm, (**B**) 20 nm, and (**C**) 60 nm (columns) in three snapshot: 6hrs, 9hrs and 12hrs (rows).
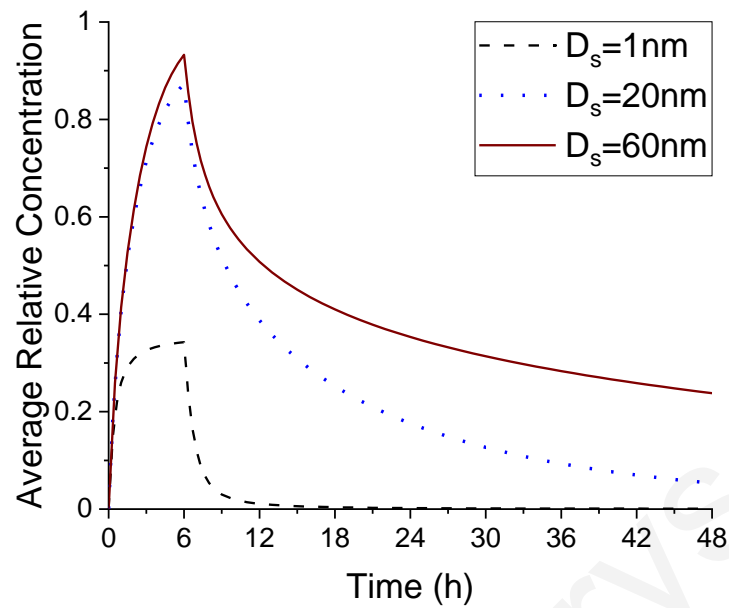
Figure 3.15: Plots of the average relative concentration in tumor tissue as a function of time for different diameters of therapeutic agents and 7.5×10^{-13} $m^2(Pa\ s)^{-1}$ hydraulic conductivity of the tumor interstitial space and 50 nm diameter of vascular wall pores.

As the pore diameter of vessel walls increases, both the interstitial fluid pressure and velocity increase too. Furthermore, the vascular permeability of drug rises with the pore diameter. Taken together, after the infusion flow, the drug concentration is decreased considerably. For 100 nm pore diameter of vessel wall, the distribution of drug with 1nm diameter remains unchanged, Figure 3.16A. After CED administration, the average relative drug concentration in tumor is negligible, Figure 3.17. The distribution of nanoparticles with 20 nm and 60 nm diameters is similar and the drug concentration decreases radially within the tumor tissue, Figure 3.16B and C. The maximum average relative concentration is 0.67 at 6 hours for 60 nm diameter of therapeutic agent, Figure 3.17.
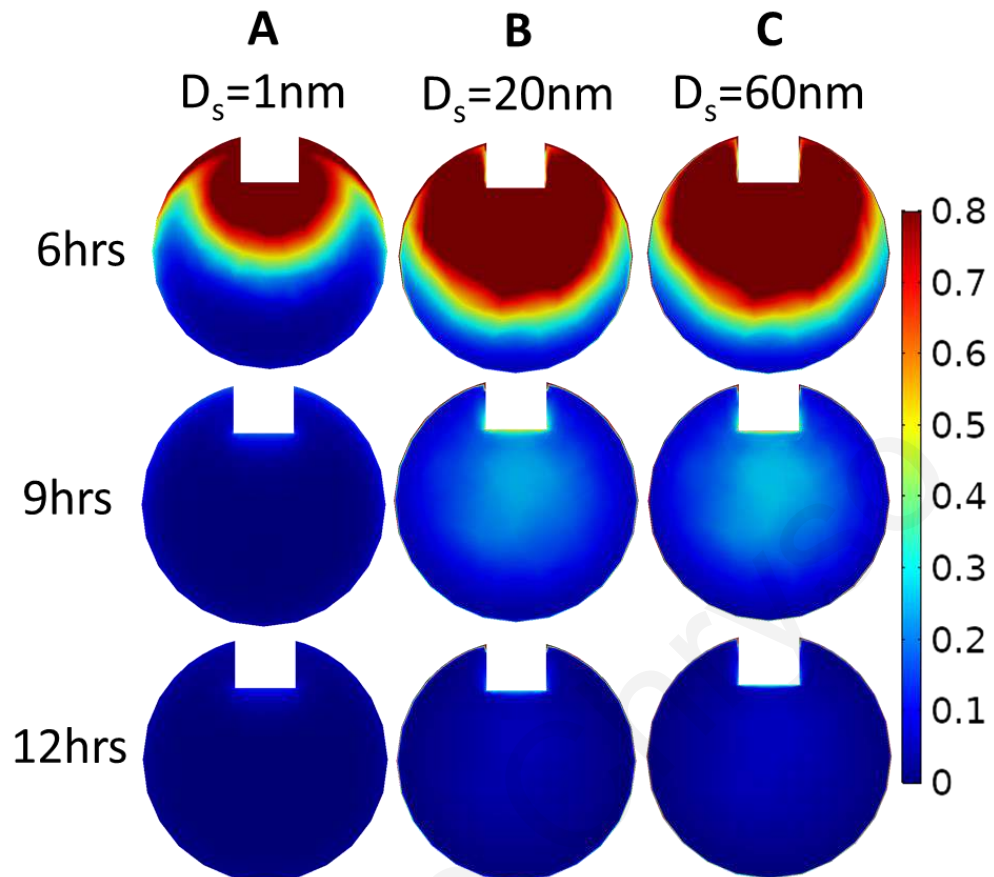
Figure 3.16: FE simulation results. A sagittal view in the center of the tumor tissue showing the spatial distribution of drug concentration for 7.5×10^{-13} m^2(Pa s)$^{-1}$ hydraulic conductivity of the tumor interstitial space, 100 nm diameter of vascular wall pores, and for different diameters of the therapeutic agent: (**A**) 1 nm, (**B**) 20 nm, and (**C**) 60 nm (columns) in three snapshot: 6hrs, 9hrs and 12hrs (rows).
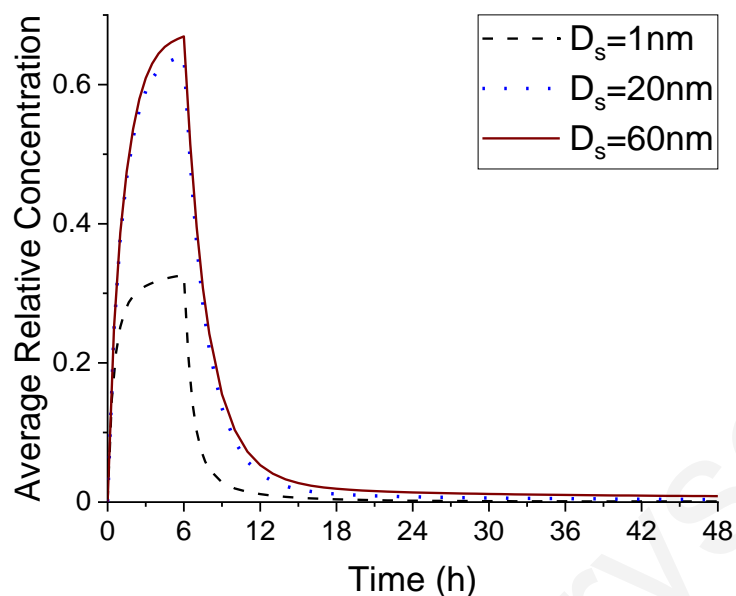
Figure 3.17: Plots of the average relative concentration in tumor tissue as a function of time for different diameters of therapeutic agents and 7.5×10^{-13} m^2(Pa s)$^{-1}$ hydraulic conductivity of the tumor interstitial space and 100 nm diameter of vascular wall pores.

Finally, the pore diameter of vessel walls is equal to 150 nm and the hydraulic conductivity of tumor interstitial space is still on the same levels. The interstitial fluid velocity increases at the tumor margin, and fluid can exit from the tumor tissue, carrying therapeutic agents. The nanoparticles with 1 nm diameter have the same spatial distribution with previous simulations, Figure 3.18A and the maximum average relative concentration of this drug is 0.31 at 6 hours, Figure 3.19. Furthermore, the spatial distribution of drug with 20 nm and 60 nm diameter is similar once again, with the maximum concentration located at center of the tumor. For 60 nm diameter, the drug concentration at the center is slightly higher compared to that of the 20 nm drug size, as shown in Figure 3.18B and C. The maximum average relative concentration is 0.63 at 6 hours for 60 nm diameter of drug, Figure 3.19.
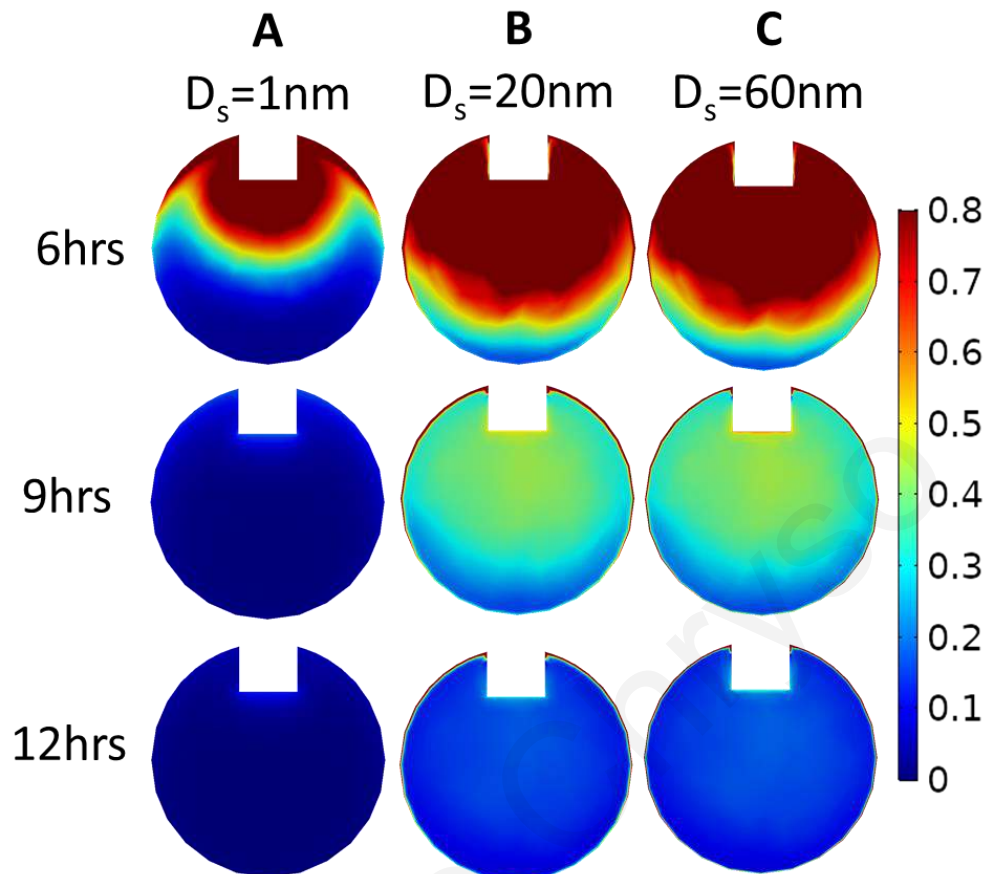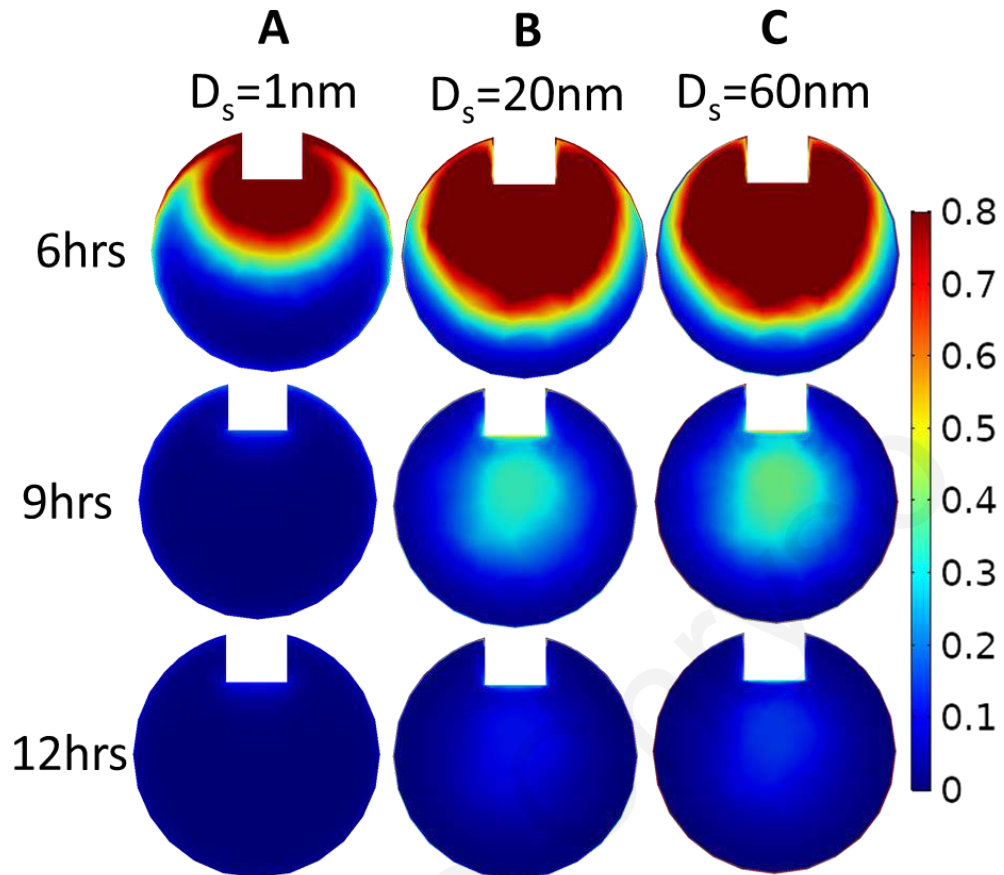
Figure 3.18: FE simulation results. A sagittal view in the center of the tumor tissue showing the spatial distribution of drug concentration for 7.5×10^{-13} m^2(Pa s)$^{-1}$ hydraulic conductivity of the tumor interstitial space, 150 nm diameter of vascular wall pores, and for different diameters of the therapeutic agent: (**A**) 1 nm, (**B**) 20 nm, and (**C**) 60 nm (columns) in three snapshot: 6hrs, 9hrs and 12hrs (rows).
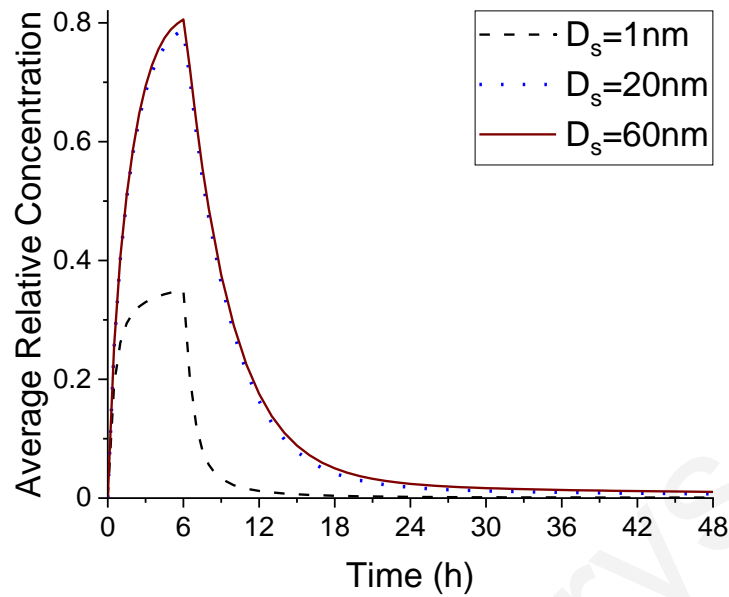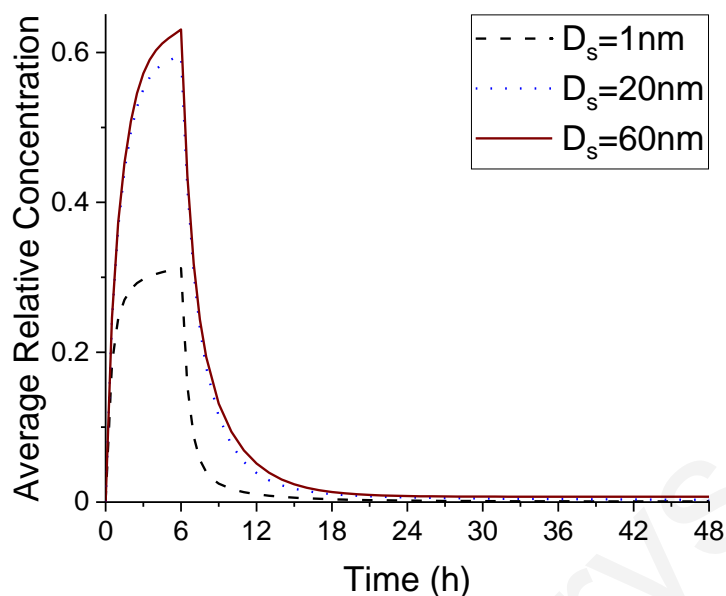
Figure 3.19: Plots of the average relative concentration in tumor tissue as a function of time for different diameters of therapeutic agents and 7.5×10^{-13} m^2(Pa s)$^{-1}$ hydraulic conductivity of the tumor interstitial space and 150 nm diameter of vascular wall pores.

For the highest hydraulic conductivity value of tumor tissue, plots of the average relative concentration of drugs are created for different diameters of vascular wall pore and for each drug size, Figure 3.20. It is detected that for 1nm drug diameter, the maximum average relative drug consecration value is slightly shifted to lower values by increasing the diameter of vascular wall pore. Moreover, for the 20 and 60 nm nanoparticles, after the infusion, the average relative concentrations decrease sharply for 100 and 150 nm pore diameter compared to the 50 nm pore diameter of the vessel wall.
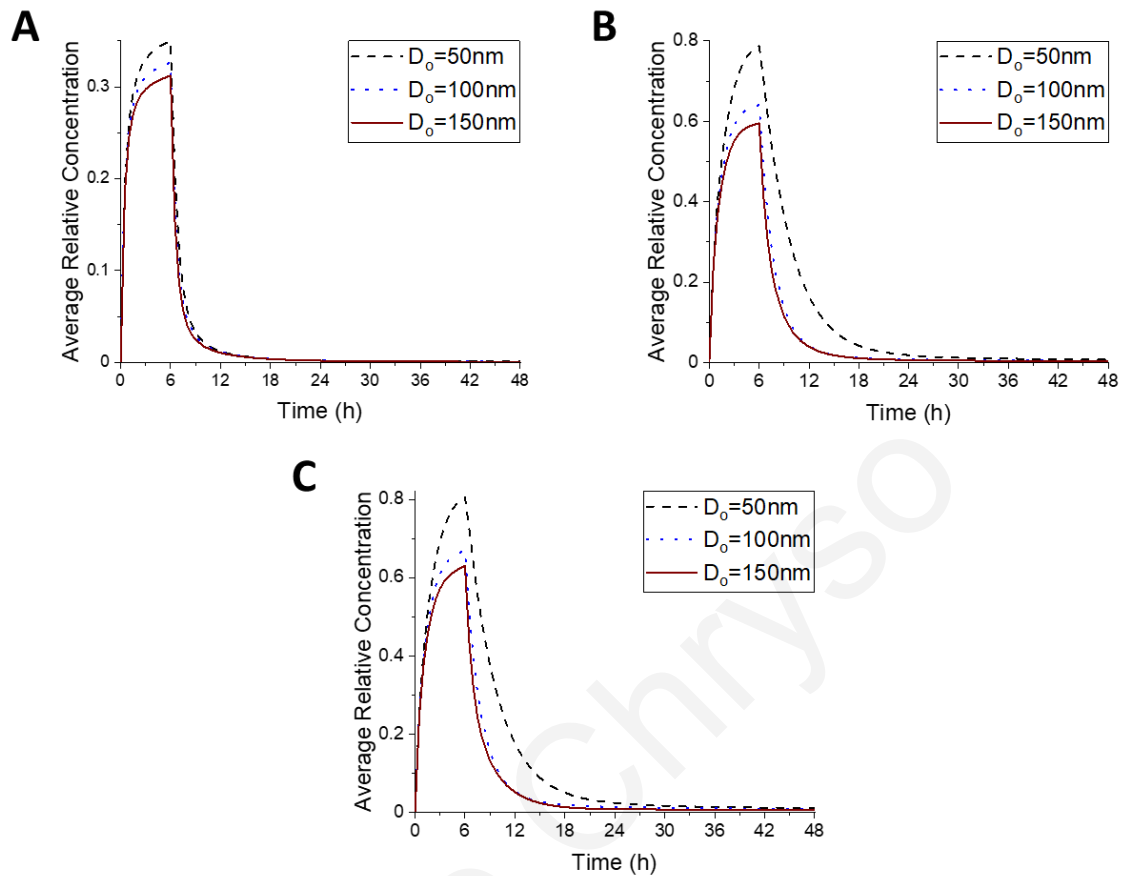
Figure 3.20: Plots of the average relative concentration in tumor tissue as a function of time for 7.5×10^{-13} m^2(Pa s)$^{-1}$ hydraulic conductivity of the tumor interstitial space and different diameters of vascular wall pores, and for different diameters of the therapeutic agent: (**A**) 1 nm, (**B**) 20 nm, and (**C**) 60 nm.

Supplementary plots of the average relative concentration of drug as a function of time are created for different values of hydraulic conductivity of tissue interstitial space and for each drug size and diameter of vessel wall pores, in Annex II. Comparing the prediction outcomes, it is observed that the average relative concentrations of drug with 1 nm diameter are insignificantly affected by changing the tissue hydraulic conductivity for each pore diameter. Besides, the average relative concentrations of both drugs with 20 and 60 nm are higher over time for the lower tissue hydraulic conductivity for each pore diameter. To conclude, these simulation series demonstrate how the spatial distribution and average relative concentration of drugs are affected by chancing pathophysiological conditions in tumor tissue and the drug sizes.

3.2.3 Heterogeneity of drug distribution

In order to investigate the heterogeneity of the drug distribution, the relative drug concentration as a function of relative distance from the tumor center is calculated for four different directions in the plane, as shown Figure 3.21. Therefore, the average relative concentration of the drug and the standard error are calculated. The standard error bars represent the heterogeneity of the drug distribution, giving a general picture of how close the results are from the average value. The smaller the error bars, the more homogeneous the distribution of the drug. The heterogeneity of the drug distribution is assessed during and after CED administration, taking snapshots at 5 hours and 9 hours. The drugs with a dimeter of 20nm and 60nm are selected for the heterogeneity measurements because the concentration distribution of the 1 nm drug is poor over time.
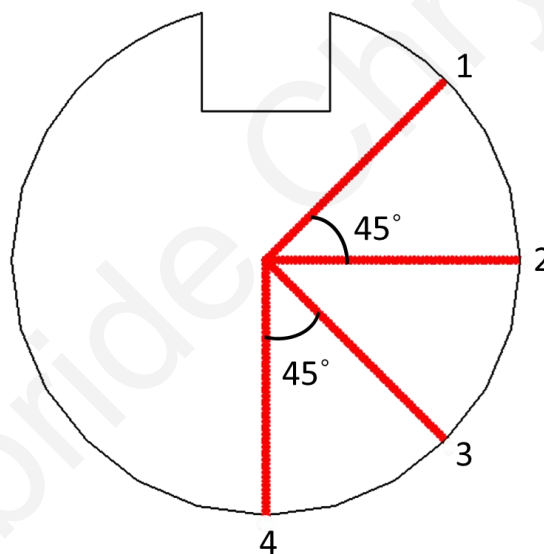
Figure 3.21: Schematic representation of four different directions in the plane for calculating both the average relative concentration of the drug and the standard error.

In Figure 3.22, the average relative concentration calculated from the four directions is illustrated as a function of the relative distance from the tumor center during and after CED for 150 nm pore diameter and 7.5×10^{-14} $m^2(Pa\ s)^{-1}$ hydraulic conductivity of tumor interstitial space. During infusion, for 20 nm drug diameter, the average relative concentration is around unit and decreases after 0.4 relative distance from the tumor center, Figure 3.22A. Similarly, the average relative concentration fluctuates around unit following a decrease after 0.5 relative distance, Figure 3.22C. According to the error bars, there is a homogeneous spatial distribution of the drug near the tumor center for both drug diameters. The heterogeneity exists radially outwards where the values of error bars increase. This happens because lines 1 and 2 are closer to

the infusion site and the drug concentration values are higher along their lines compared to lines 3 and 4, Figure 3.21. After infusion, the average relative concentrations for both drug sizes gradually decrease as a function of the relative distance. The spatial distribution drug is homogeneous, Figure 3.22B and D, and this is verified from Figure 3.11B and C.
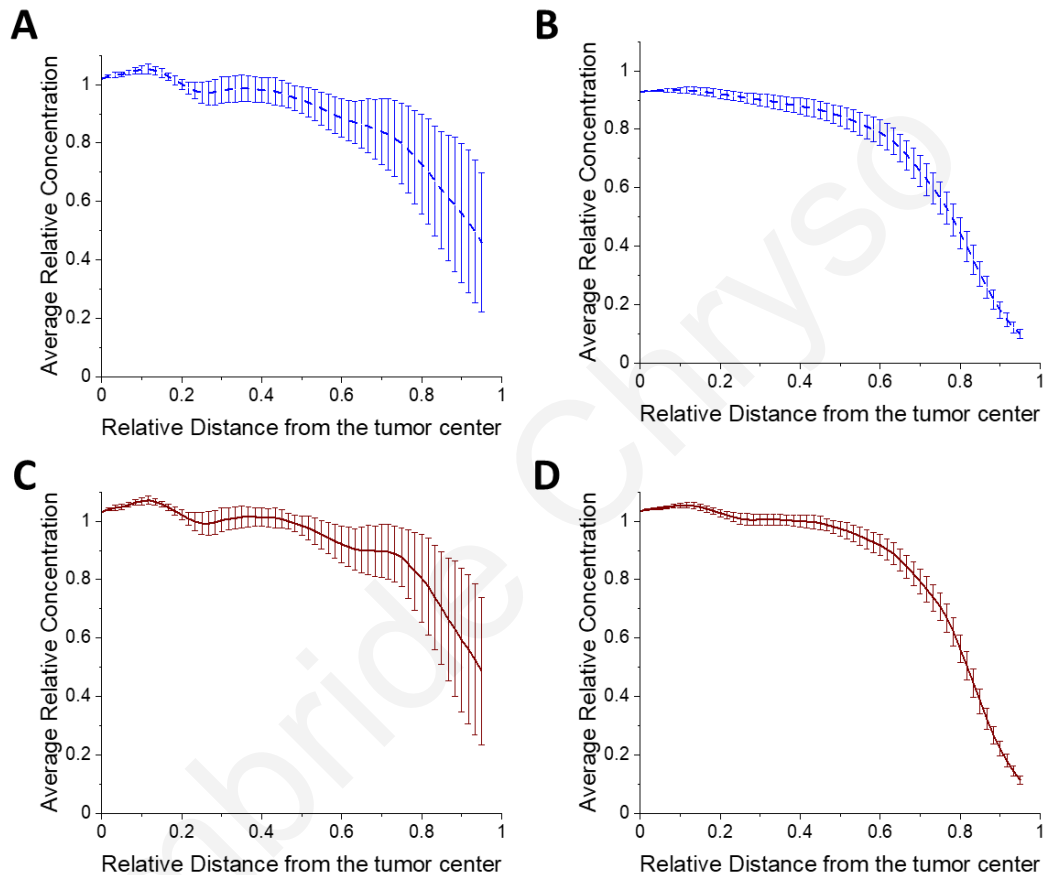
Figure 3.22: Plots of the average relative concentration calculated from the four directions as a function of the relative distance from the tumor center **(A, C)** after 5hrs **(B, D)** after 9 hrs, for 150 nm diameter of vascular pore size and 7.5×10^{-14} m^2(Pa s)$^{-1}$ hydraulic conductivity of the tumor interstitial space, and for different drug diameters: **(A, B)** 20 nm and **(C, D)** 60nm.

By increasing the hydraulic conductivity of the tumor interstitial space, the heterogeneity of the drug distribution is affected significantly during CED, as shown Figure 3.23A and C. For both drug sizes, the average relative concentrations gradually decrease and the heterogeneity appears from 0.3 relative distance from the tumor center. However, after the infusion flow, the spatial distribution drug is homogeneous for both drug sizes, Figure 3.23B and D. It is observed from Figure 3.22 and Figure 3.23 that the heterogeneity of the drug distribution and the average relative drug concentration are similar for both drug sizes by comparing separately the plots during and after CED for

each pathological conditions of the tumor. Moreover, in Annex III, every other graph showing the heterogeneity of each drug using different tumor microenvironment properties are presented.
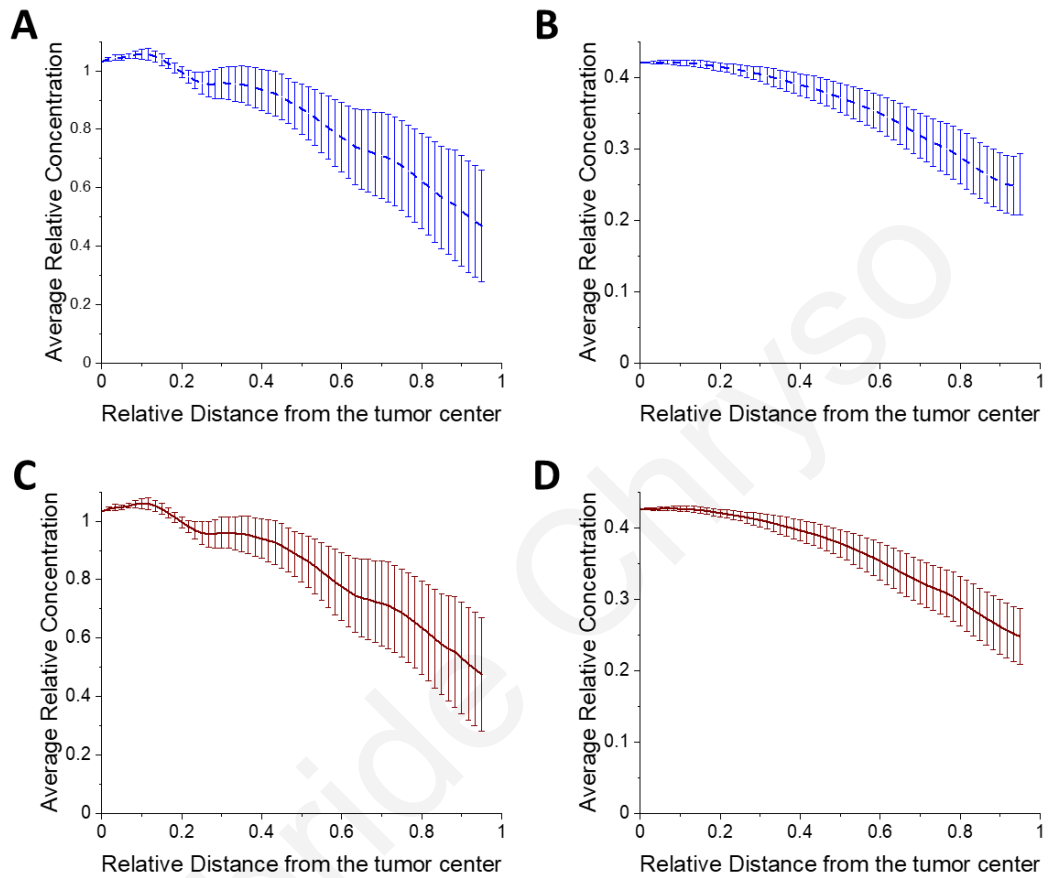
Figure 3.23: Plots of the average relative concentration calculated from the four directions as a function of the relative distance from the tumor center **(A, C)** after 5hrs **(B, D**) after 9 hrs, for 50 nm diameter of vascular pore size and 7.5×10^{-13} m^2(Pa s)$^{-1}$ hydraulic conductivity of the tumor interstitial space, and for different drug diameter: **(A, B)** 20 nm and **(C, D)** 60nm.

3.3 Validation of predictive outcomes

In cases in which experimental data are difficult to obtain, a mathematical model can provide useful information, as long as it can be validated. These predictive results need to be validated to offer further insights of the spatial distribution and the average drug concentration in the tumor, proposing an effective treatment of brain cancer. The tumor IFP and IFV profiles after CED can be confirmed according to the present literature [6, 43]. Additionally, the relation between the tumor interstitial fluid pressure and the tumor microenvironment properties is confirmed from previous simulation studies [43]. The range of the tumor interstitial fluid velocity values agrees with the experimental data which show that the magnitude of fluid velocity varies from 10^{-7} to 10^{-6} m/s in the brain tissue [44-46]. Besides, it is challenging to confirm experimentally the predicted distribution of drug concentration in the human brain tissue during CED. Consequently, the validation of the IFP and IFV profiles is essential to confirm the spatial distribution of the drug in CED treatments. In addition, the calculated tumor tissue properties, *i.e.*, the vascular permeability of the drug and the hydraulic conductivity of the vascular wall, using the theory for hindered transport of rigid solutes are verified from the literature [37, 47, 48].

Chapter 4

4 CONCLUSIONS

4.1 <u>C o n c l u s i o n s</u>

This Master Thesis focuses on the biomechanical and biotransport aspect of convection-enhanced delivery (CED). The project develops a mathematical and computational model for brain cancer treatment to predict the drug concentration distributions, applying engineering and physical sciences principles to medicine. Therefore, this *in silico* study investigates the drug concentration during and after CED of different drug sizes by changing the pathophysiological conditions of the tumor tissue. The therapeutic agents of 1, 20 and 60 nm in diameter and vessel wall pores of tumor tissue with diameters 50, 100 and 150 nm have been considered. Also, the hydraulic conductivity of the tumor interstitial space is taken equal to 7.5×10^{-14} and 7.5×10^{-13} $m^2(Pa\ s)^{-1}$. A series of simulations have been performed to fully comprehend the fluid dynamics and the distribution of the drug concentration as a function of the drug physiochemical and tumor microenvironment properties. Additionally, the heterogeneity of the drug distribution has been extensively examined.

The *in silico* predicted IFP and IFV profiles of the tumor tissue are validated from the existent literature. The predictive outcomes show that the tumor IFP can be decreased by increasing hydraulic conductivity of the tumor interstitial space and/or by lowering pore diameter of the vascular wall of the tumor tissue. Moreover, for a given hydraulic conductivity of the tumor interstitial space, the IFV value at the tumor margin can be lowered by decreasing the pore diameter of the vascular wall. Increasing tissue hydraulic conductivity causes higher fluid velocities within the tumor tissue. Additionally, during CED, the peak pressure and velocity are achieved at the infusion site, and the values decrease rapidly towards the tumour surface.

Regarding the drug distribution, the maximum average relative concentration of the drug occurs at 6 hours when the infusion flow stops. The distribution and the average concentration of the nanoparticles with 1nm diameter are affected insignificantly by changing the pathophysiological conditions of tumor tissue. When considering the

highest value of the hydraulic conductivity of the tumor interstitial space, changing the drug diameter from 20 to 60 nm the drug distribution and average relative concentration are not sensitive for a given pore diameter of vessel wall. The predictive results of the drug with 60 nm diameter are promising and remarkable for the lowest value of the hydraulic conductivity of the tumor interstitial space and 150 nm pore diameter of vascular wall. Under this tumor microenvironment properties, this therapeutic agent is evenly distributed within the tumor interstitial space during and after CED. Specifically, the drug spatial distribution is extremely homogeneous after CED, as shown in Figure 3.22. The average relative concentration of this drug remains at high levels during a day with the maximum drug concentration located at the center. However, the predictive tumor IFP is high at the infusion site during CED, which is a drawback for this condition. Alternatively, for lower tumor IFP, in the case of the highest hydraulic conductivity of the tumor interstitial and 50 nm pore diameter, good prediction of the spatial distribution and the average relative concentration of the drug with both 20 and 60 nm diameter is observed. Nonetheless, there is faster drug release from the tumor tissue. From the heterogeneity of drug distribution point of view, during CED the drug distribution is not homogenous across the tumor periphery. While, after CED the drug distribution is considerably homogenous along the entire tumor.

Additionally, several assumptions have been considered to simplify the mathematical and computational model. The drug is considered a spherical nanoparticle and the vascular wall openings are modeled as cylinder pores. Therefore, the theory for hindered transport of rigid solutes through liquid filled pores can be applied to describe drug transport across the tumor vessel walls. Moreover, the rate of the drug decomposition is not defined in this model because the main focus is to correlate the drug distribution with the tumor microenvironment properties and the drug size. Regarding the limitations, the model incorporates only biomechanical properties of both the grey and white matter. It does not account for other structural components of the brain such as ventricle, cavities. Therefore, using MR images, the detection of sharp boundaries and surfaces of the brain substructures is necessary for the three-dimensional reconstruction of the brain geometry. How incorporation of these components would affect the simulations is not intuitive and detailed simulations would have to be performed. Also, according to the literature [49, 50], the drug transport efficiency varies greatly in different regions of the brain. The drug transport in the gray matter is isotropic, whereas white matter have anisotropic diffusion and heterogenetic properties.

Hence, diffusion tensor imaging (DTI) could be used to measure the tissue anisotropy, providing an accurate estimation of the effective diffusivity and its distribution within the entire brain.

To conclude, adjusting the tumor microenvironment properties prior to the drug administration *via* CED may provide better conditions for the drug delivery within the tumor tissue, minimizing drug exposure to healthy tissue. These predictive outcomes provide further and useful insights of the spatial distribution and the average drug concentration in the tumor towards an effective treatment of brain cancer.

4.2 Proposals for further investigation

Based on the thesis results, it is predicted that the spatial distribution of drug with 1nm diameter is poor and the average relative drug concentration in tumor tissue is lower compared to other drug sizes. Consequently, the delivery of a nanoparticle carrier containing and releasing chemotherapy is important to be studied in the near future, in order to investigate the effectiveness of drug delivery. Additionally, in this study, the catheter is considered to be located inside the tumor tissue. In order to investigate the effect of the catheter placement on drug delivery, a series of simulations will be carried out where catheter is located outside of the tumor tissue. Sometimes in clinical situations, physicians are not able to inject the drug directly into the tumor, and thus they are forced to place the catheter near the tumor tissue.

References

[1]   T. Stylianopoulos, L. L. Munn, and R. K. Jain, "Reengineering the Physical Microenvironment of Tumors to Improve Drug Delivery and Efficacy: From Mathematical Modeling to Bench to Bedside," *Trends Cancer,* vol. 4, pp. 292-319, Apr 2018.

[2]   J. D. Martin, D. Fukumura, D. G. Duda, Y. Boucher, and R. K. Jain, "Reengineering the Tumor Microenvironment to Alleviate Hypoxia and Overcome Cancer Heterogeneity," *Cold Spring Harb Perspect Med,* vol. 6, Dec 1 2016.

[3]   P. A. Netti, D. A. Berk, M. A. Swartz, A. J. Grodzinsky, and R. K. Jain, "Role of extracellular matrix assembly in interstitial transport in solid tumors," *Cancer Res,* vol. 60, pp. 2497-503, 2000.

[4]   C. C. Michel, T. E. Woodcock, and F. E. Curry, "Understanding and extending the Starling principle," *Acta Anaesthesiol Scand,* vol. 64, pp. 1032-1037, Sep 2020.

[5]   R. K. Jain, "Transport of molecules across tumor vasculature," *Cancer Metastasis Rev,* vol. 6, pp. 559-93, 1987.

[6]   L. T. Baxter and R. K. Jain, "Transport of fluid and macromolecules in tumors. I. Role of interstitial pressure and convection," *Microvasc Res,* vol. 37, pp. 77-104, 1989.

[7]   Y.-E. L. Koo, G. R. Reddy, M. Bhojani, R. Schneider, M. A. Philbert, A. Rehemtulla*, et al.*, "Brain cancer diagnosis and therapy with nanoplatforms," *Advanced drug delivery reviews,* vol. 58, pp. 1556-1577, 2006.

[8]   A. M. Mehta, A. M. Sonabend, and J. N. Bruce, "Convection-Enhanced Delivery," *Neurotherapeutics,* vol. 14, pp. 358-371, Apr 2017.

[9]   M. Shi and L. Sanche, "Convection-Enhanced Delivery in Malignant Gliomas: A Review of Toxicity and Efficacy," *J Oncol,* vol. 2019, p. 9342796, 2019.

[10]   G. Li, W. Yuan, and B. M. Fu, "A model for the blood-brain barrier permeability to water and small solutes," *J Biomech,* vol. 43, pp. 2133-40, Aug 10 2010.

[11]   C. D. Arvanitis, G. B. Ferraro, and R. K. Jain, "The blood-brain barrier and blood-tumour barrier in brain tumours and metastases," *Nat Rev Cancer,* vol. 20, pp. 26-41, Jan 2020.

[12]   S. D. Ferguson, K. Foster, and B. Yamini, "Convection-enhanced delivery for treatment of brain tumors," *Expert Rev Anticancer Ther,* vol. 7, pp. S79-85, Dec 2007.

[13]   T. A. Juratli, G. Schackert, and D. Krex, "Current status of local therapy in malignant gliomas--a clinical review of three selected approaches," *Pharmacol Ther,* vol. 139, pp. 341-58, Sep 2013.

[14]   R. Pandit, L. Chen, and J. Gotz, "The blood-brain barrier: Physiology and strategies for drug delivery," *Adv Drug Deliv Rev,* vol. 165-166, pp. 1-14, 2020.

[15]   E. Lueshen, K. Tangen, A. I. Mehta, and A. Linninger, "Backflow-free catheters for efficient and safe convection-enhanced delivery of therapeutics," *Med Eng Phys,* vol. 45, pp. 15-24, Jul 2017.

[16]   R. H. Bobo, D. W. Laske, A. Akbasak, P. F. Morrison, R. L. Dedrick, and E. H. Oldfield, "Convection-enhanced delivery of macromolecules in the brain," *Proc Natl Acad Sci U S A,* vol. 91, pp. 2076-80, Mar 15 1994.

[17]   T. Tykocki and G. Miekisiak, "Application of Convection-Enhanced Drug Delivery in the Treatment of Malignant Gliomas," *World Neurosurg,* vol. 90, pp. 172-178, Jun 2016.

[18]   E. Allard, C. Passirani, and J. P. Benoit, "Convection-enhanced delivery of nanocarriers for the treatment of brain tumors," *Biomaterials,* vol. 30, pp. 2302-18, Apr 2009.

[19]   A. Jahangiri, A. T. Chin, P. M. Flanigan, R. Chen, K. Bankiewicz, and M. K. Aghi, "Convection-enhanced delivery in glioblastoma: a review of preclinical and clinical studies," *J Neurosurg,* vol. 126, pp. 191-200, Jan 2017.

[20]   R. Raghavan, M. L. Brady, M. I. Rodriguez-Ponce, A. Hartlep, C. Pedain, and J. H. Sampson, "Convection-enhanced delivery of therapeutics for brain disease, and its optimization," *Neurosurg Focus,* vol. 20, p. E12, Apr 15 2006.

[21]   K. H. Støverud, M. Darcis, R. Helmig, and S. M. Hassanizadeh, "Modeling concentration distribution and deformation during convection-enhanced drug delivery into brain tissue," *Transport in porous media,* vol. 92, pp. 119-143, 2012.

[22]   L. H. Antoine, R. P. Koomullil, T. M. Wick, L. B. Nabors, A. K. A. Aal, and M. S. Bolding, "Catheter placement selection for convection-enhanced delivery of therapeutic agents to brain tumors," *F1000Research,* vol. 9, p. 1415, 2020.

[23]   G. A. Orozco, J. H. Smith, and J. J. Garcia, "Three-dimensional nonlinear finite element model to estimate backflow during flow-controlled infusions into the brain," *Proc Inst Mech Eng H,* vol. 234, pp. 1018-1028, Sep 2020.

[24]   A. A. Linninger, M. R. Somayaji, M. Mekarski, and L. Zhang, "Prediction of convection-enhanced drug delivery to the human brain," *J Theor Biol,* vol. 250, pp. 125-38, Jan 7 2008.

[25]   A. A. Linninger, M. R. Somayaji, L. Zhang, M. Smitha Hariharan, and R. D. Penn, "Rigorous mathematical modeling techniques for optimal delivery of macromolecules to the brain," *IEEE Trans Biomed Eng,* vol. 55, pp. 2303-13, Sep 2008.

[26]   W. Zhan, D. Y. Arifin, T. K. Lee, and C. H. Wang, "Mathematical Modelling of Convection Enhanced Delivery of Carmustine and Paclitaxel for Brain Tumour Therapy," *Pharm Res,* vol. 34, pp. 860-873, Apr 2017.

[27]   W. Zhan and C. H. Wang, "Convection enhanced delivery of chemotherapeutic drugs into brain tumour," *J Control Release,* vol. 271, pp. 74-87, Feb 10 2018.

[28]   W. Zhan and C. H. Wang, "Convection enhanced delivery of liposome encapsulated doxorubicin for brain tumour therapy," *J Control Release,* vol. 285, pp. 212-229, Sep 10 2018.

[29]   W. Zhan, Y. B. F. Rodriguez, and D. Dini, "Effect of tissue permeability and drug diffusion anisotropy on convection-enhanced delivery," *Drug Deliv,* vol. 26, pp. 773-781, Dec 2019.

[30]   W. Zhan, "Convection enhanced delivery of anti-angiogenic and cytotoxic agents in combination therapy against brain tumour," *Eur J Pharm Sci,* vol. 141, p. 105094, Jan 1 2020.

[31]   S. Angeli and T. Stylianopoulos, "Biphasic modeling of brain tumor biomechanics and response to radiation treatment," *J Biomech,* Mar 30 2016.

[32]   W. M. Deen, "Hindered Transport of Large molecules in Liquid-Filled Pores," *AIChE J,* vol. 33, pp. 1409-1425, 1987.

[33]   D. A. Nield and A. Bejan, *Convection in porous media*, 2nd ed. New York: Springer, 1999.

[34]   F. Mpekris, S. Angeli, A. P. Pirentis, and T. Stylianopoulos, "Stress-mediated progression of solid tumors: effect of mechanical stress on tissue oxygenation,

cancer cell proliferation, and drug delivery," *Biomech Model Mechanobiol,* vol. 14, pp. 1391-402, Nov 2015.

[35]   F. Mpekris, J. W. Baish, T. Stylianopoulos, and R. K. Jain, "Role of vascular normalization in benefit from metronomic chemotherapy," *Proc Natl Acad Sci U S A,* vol. 114, pp. 1994-1999, Feb 21 2017.

[36]   COMSOL 5.4., *CFD Module User's Guide*: COMSOL, 2018.

[37]   S. K. Hobbs, W. L. Monsky, F. Yuan, W. G. Roberts, L. Griffith, V. P. Torchilin*, et al.*, "Regulation of transport pathways in tumor vessels: role of tumor type and microenvironment," *Proc Natl Acad Sci U S A,* vol. 95, pp. 4607-12, 1998.

[38]   H. Sarin, A. S. Kanevsky, H. Wu, A. A. Sousa, C. M. Wilson, M. A. Aronova*, et al.*, "Physiologic upper limit of pore size in the blood-tumor barrier of malignant solid tumors," *J Transl Med,* vol. 7, p. 51, Jun 23 2009.

[39]   N. U. Barua, S. P. Lowis, M. Woolley, S. O'Sullivan, R. Harrison, and S. S. Gill, "Robot-guided convection-enhanced delivery of carboplatin for advanced brainstem glioma," *Acta Neurochir (Wien),* vol. 155, pp. 1459-65, Aug 2013.

[40]   C. A. Stine and J. M. Munson, "Convection-Enhanced Delivery: Connection to and Impact of Interstitial Fluid Flow," *Front Oncol,* vol. 9, p. 966, 2019.

[41]   U. Tosi and M. Souweidane, "Convection Enhanced Delivery for Diffuse Intrinsic Pontine Glioma: Review of a Single Institution Experience," *Pharmaceutics,* vol. 12, Jul 14 2020.

[42]   A. Pluen, Y. Boucher, S. Ramanujan, T. D. McKee, T. Gohongi, E. di Tomaso*, et al.*, "Role of tumor-host interactions in interstitial diffusion of macromolecules: cranial vs. subcutaneous tumors," *Proc Natl Acad Sci U S A,* vol. 98, pp. 4628-33, 2001.

[43]   R. K. Jain, R. T. Tong, and L. L. Munn, "Effect of vascular normalization by antiangiogenic therapy on interstitial hypertension, peritumor edema, and lymphatic metastasis: insights from a mathematical model," *Cancer Res,* vol. 67, pp. 2729-35, 2007.

[44]   A. B. Fleming and W. M. Saltzman, "Pharmacokinetics of the carmustine implant," *Clin Pharmacokinet,* vol. 41, pp. 403-19, 2002.

[45]   L. K. Fung, M. Shin, B. Tyler, H. Brem, and W. M. Saltzman, "Chemotherapeutic drugs released from polymers: distribution of 1,3-bis(2-chloroethyl)-1-nitrosourea in the rat brain," *Pharm Res,* vol. 13, pp. 671-82, May 1996.

[46]   H. K. Kimelberg, "Water homeostasis in the brain: basic concepts," *Neuroscience,* vol. 129, pp. 851-60, 2004.

[47]   J. P. Scallan and V. H. Huxley, "In vivo determination of collecting lymphatic vessel permeability to albumin: a role for lymphatics in exchange," *J Physiol,* vol. 588, pp. 243-54, Jan 1 2010.

[48]   M. R. Dreher, W. Liu, C. R. Michelich, M. W. Dewhirst, F. Yuan, and A. Chilkoti, "Tumor vascular permeability, accumulation, and penetration of macromolecular drug carriers," *J Natl Cancer Inst,* vol. 98, pp. 335-44, Mar 1 2006.

[49]   J. S. Shimony, R. C. McKinstry, E. Akbudak, J. A. Aronovitz, A. Z. Snyder, N. F. Lori*, et al.*, "Quantitative diffusion-tensor anisotropy brain MR imaging: normative human data and anatomic analysis," *Radiology,* vol. 212, pp. 770-84, Sep 1999.

[50]   Y. Cao, S. Whalen, J. Huang, K. L. Berger, and M. C. DeLano, "Asymmetry of subinsular anisotropy by in vivo diffusion tensor imaging," *Hum Brain Mapp,* vol. 20, pp. 82-90, Oct 2003.

[51]   J. Wang, Z. Lu, Y. Gao, M. G. Wientjes, and J. L. Au, "Improving delivery and efficacy of nanomedicines in solid tumors: role of tumor priming," *Nanomedicine (Lond),* vol. 6, pp. 1605-20, Nov 2011.

[52]   C. Voutouri and T. Stylianopoulos, "Evolution of osmotic pressure in solid tumors," *J Biomech,* vol. 47, pp. 3441-7, Nov 7 2014.

[53]   T. Stylianopoulos, J. D. Martin, M. Snuderl, F. Mpekris, S. R. Jain, and R. K. Jain, "Coevolution of solid stress and interstitial fluid pressure in tumors during progression: Implications for vascular collapse," *Cancer research,* vol. 73, pp. 3833-3841, 2013.

[54]   G. Kesmarky, P. Kenyeres, M. Rabai, and K. Toth, "Plasma viscosity: a forgotten variable," *Clin Hemorheol Microcirc,* vol. 39, pp. 243-6, 2008.

Annexes

Annexes I – Model Parameters

Table 1: Constant Coefficients *a* and *b* for determining the coefficients K_t and K_s, respectively [32].

Constant Coefficient	**Value**
a_1	−73/60
a_2	77.293/50.400
a_3	−22.5083
a_4	−5.617
a_5	−0.3363
a_6	−1.216
a_7	1.647
b_1	7/60
b_2	−2.227/50.400
b_3	4.0180
b_4	−3.9788
b_5	−1.9215
b_6	4.392
b_7	5.006

Table 2: Values of all parameters used in the CED brain model**.**

*Normal tissue includes Gray and White Matter.

Parameter	Description	Domain	Value	Reference
r_s	Drug radius	-	0.5, 10, 30 nm	[7, 18]
r_o	Vascular wall pore radius	Normal tissue	3.5 nm	[37, 38, 51]
		Tumor tissue	25, 50, 75 nm	
D_i	Drug diffusion coefficient	All tissues	3.49×10^{-10} m²/s for 1nm drug radius, 9.28×10^{-12} m²/s for 10nm drug radius, 3.28×10^{-12} m²/s for 30nm drug radius	[42]
k	Hydraulic conductivity of tissue interstitial space	Gray Matter	7.76×10^{-18} m²(Pa s)$^{-1}$	[3, 31]
		White Matter	7.76×10^{-16} m²(Pa s)$^{-1}$	
		Tumor tissue	7.5×10^{-14} m²(Pa s)$^{-1}$ 7.5×10^{-13} m²(Pa s)$^{-1}$	
S_v	Vascular density of blood vessels	Normal tissue	70 (cm)$^{-1}$	[35, 43]
		Tumor tissue	50 (cm)$^{-1}$	
$L_{pl}S_{vl}$	Permeability of Lymphatics	Normal tissue	3.75×10^{-4} (Pa·s)$^{-1}$	[6, 52]
		Tumor tissue	0	
γ	Fraction of vessel wall surface area occupied by pores	Normal tissue	1×10^{-3}	[35]
		Tumor tissue	1×10^{-4}	
C_v	Vascular drug concentration	All tissues	0	-
p_v	Vascular pressure of blood vessels	All tissues	2.0 kPa	[1]
p_l	Vascular pressure of lymphatic vessels	All tissues	0.0 kPa	[52]
L_{vw}	Vessel wall thickness	All tissues	5×10^{-6} m	[53]
T	Temperature	Catheter	298 K	[24, 35]
		All tissues	310 K	
μ	Water viscosity	Catheter	0.89 mPa·s	[53, 54]
	Plasma viscosity	All tissues	1.30 mPa·s	
ρ	Water density	Catheter	998 kg/m³	-
	Plasma density	All tissues	1025 kg/m³	
ε_p	Tissue porosity	All tissues	0.3	[24]

Annexes II – Supplementary plots of the average relative concentration in tumor tissue
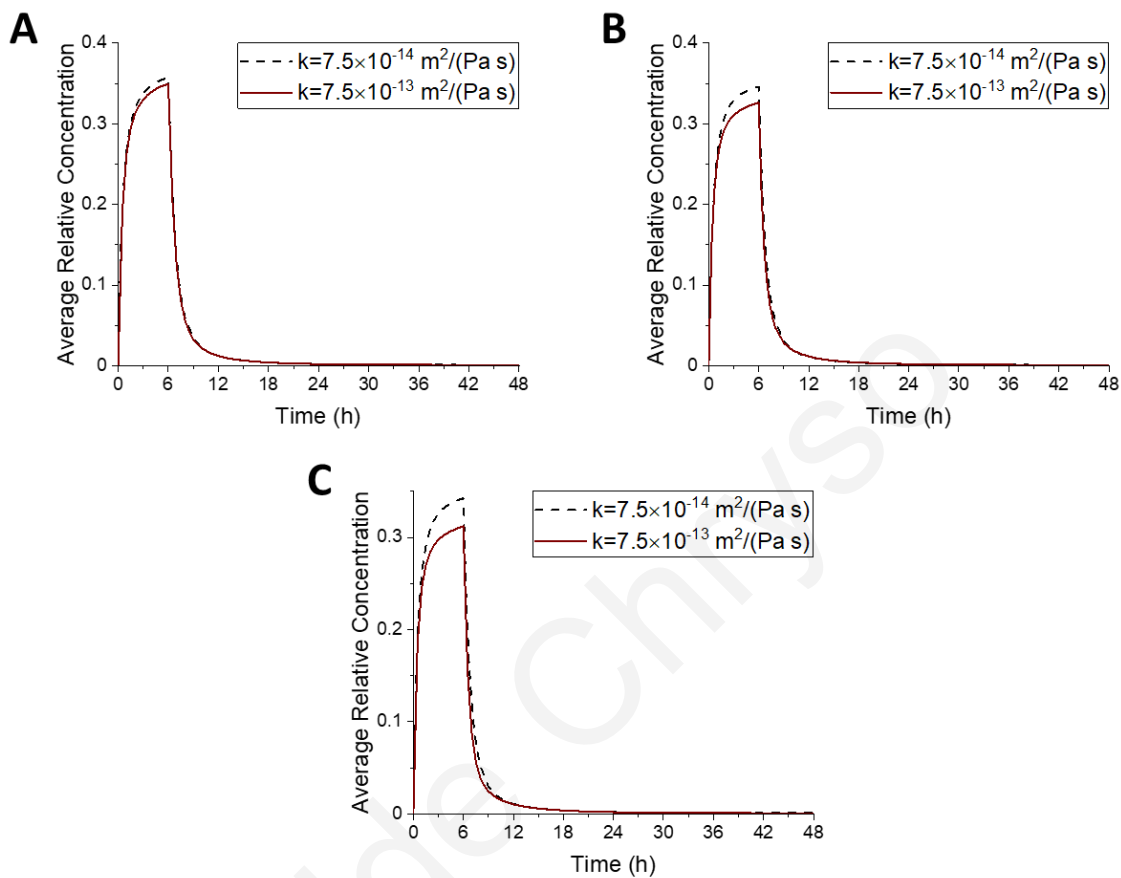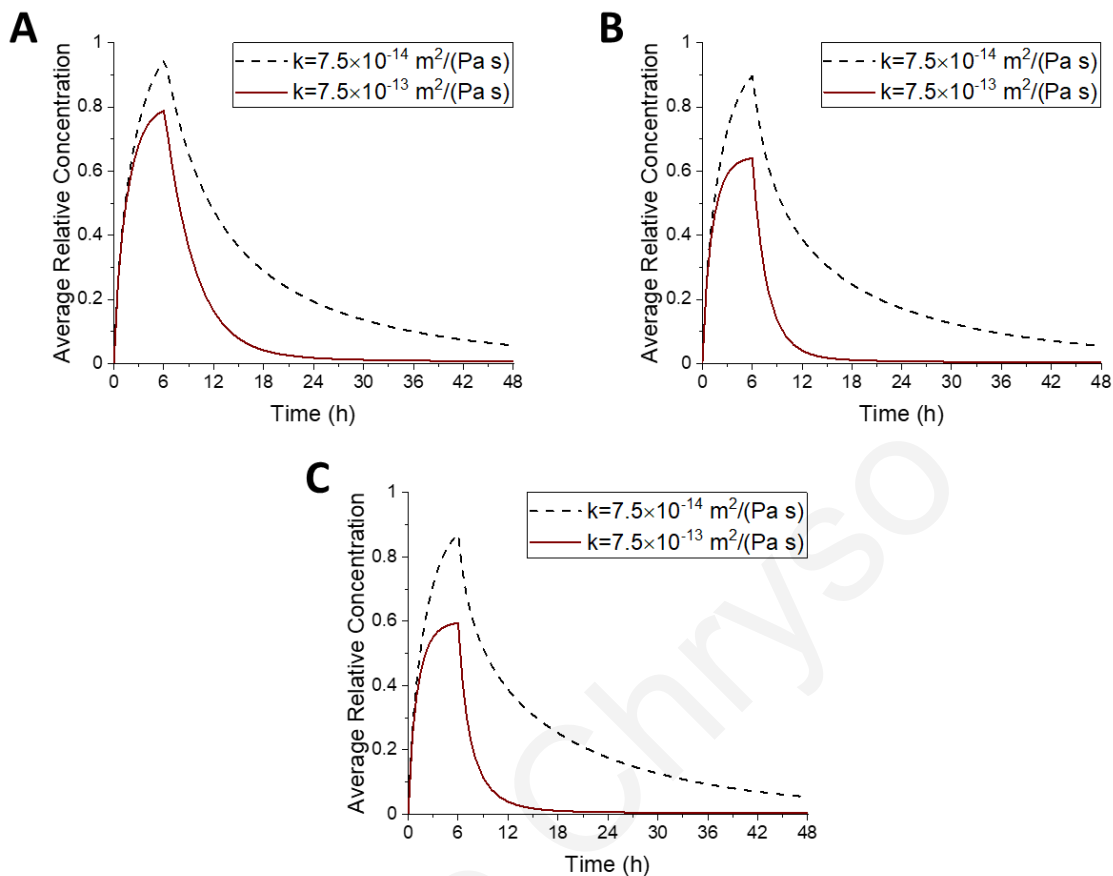

Figure 1: Plots of the average relative concentration in tumor tissue as a function of time for 1 nm diameters of therapeutic agent and different values of hydraulic conductivity of the tumor interstitial space, and for different diameters of vascular wall pores: (**A**) 50 nm, (**B**) 100 nm, and (**C**) 150 nm.
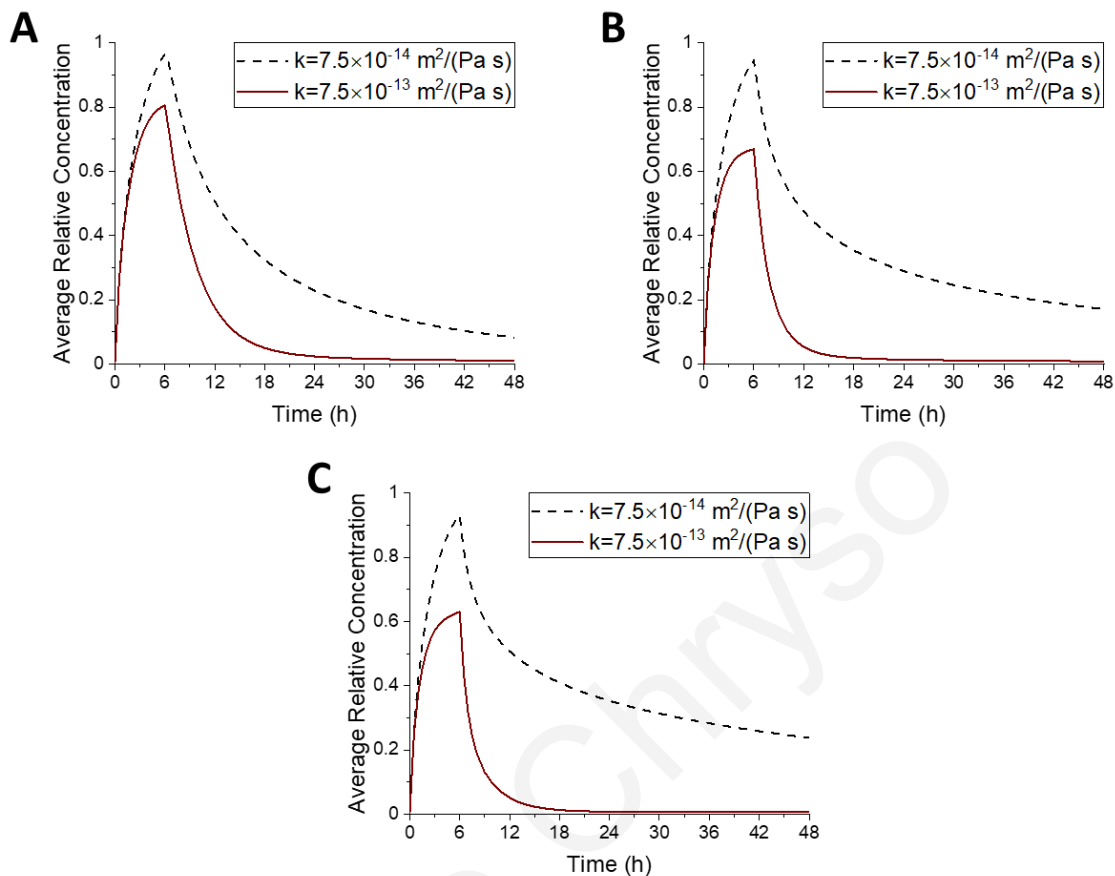
Figure 2: Plots of the average relative concentration in tumor tissue as a function of time for 20 nm diameters of therapeutic agent and different values of hydraulic conductivity of the tumor interstitial space, and for different diameters of vascular wall pores: (**A**) 50 nm, (**B**) 100 nm, and (**C**) 150 nm.

Figure 3: Plots of the average relative concentration in tumor tissue as a function of time for 60 nm diameters of therapeutic agent and different values of hydraulic conductivity of the tumor interstitial space, and for different diameters of vascular wall pores: (**A**) 50 nm, (**B**) 100 nm, and (**C**) 150 nm.

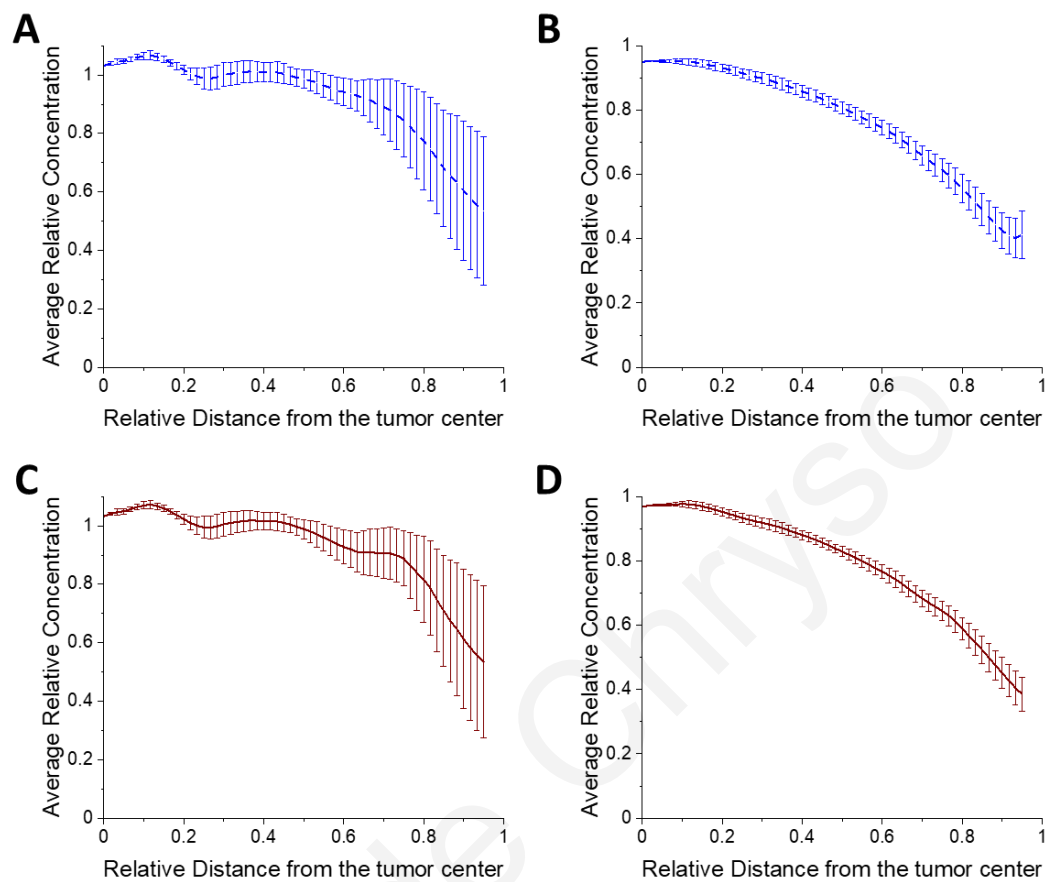**Annexes III – Supplementary plots of the heterogeneity of the drug distribution**
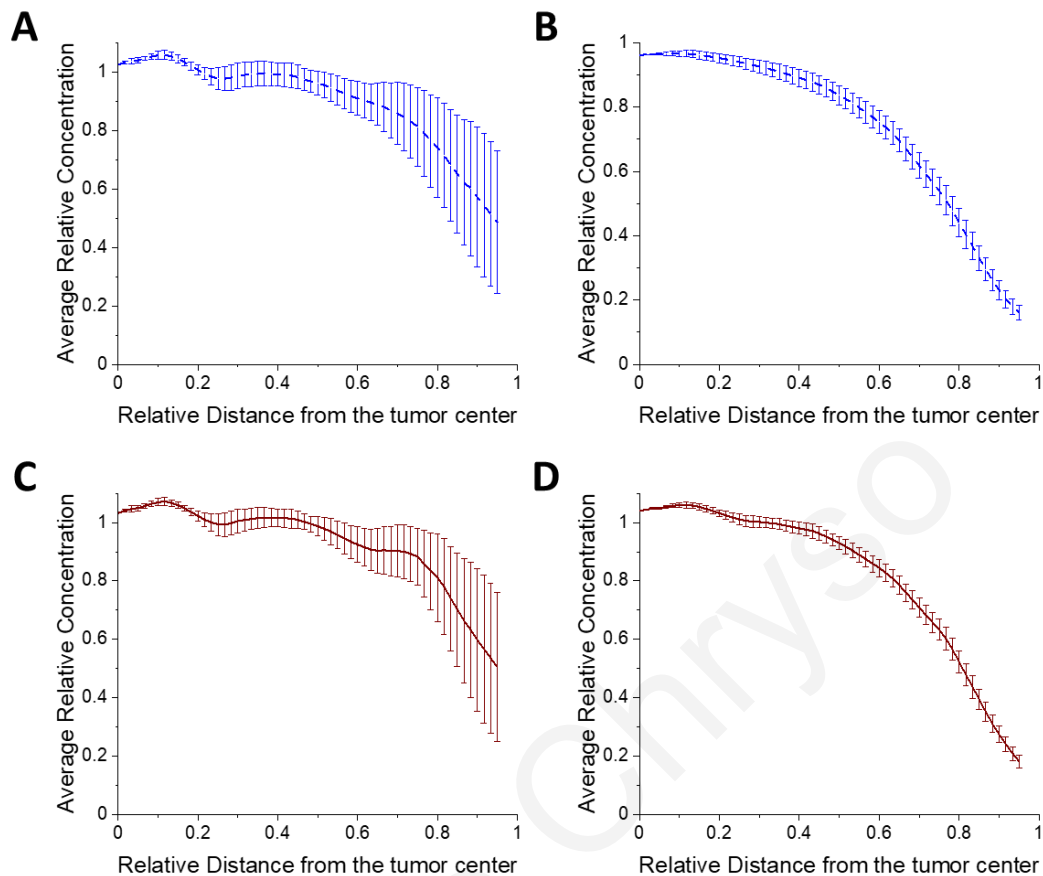

Figure 4: Plots of the average relative concentration calculated from the four directions as a function of the relative distance from the tumor center **(A, C)** after 5hrs **(B, D)** after 9 hrs, for 50 nm diameter of vascular pore size and 7.5×10^{-14} m^2(Pa s)$^{-1}$ hydraulic conductivity of the tumor interstitial space, and for different drug diameter: **(A, B)** 20 nm and **(C, D)** 60nm.

Figure 5: Plots of the average relative concentration calculated from the four directions as a function of the relative distance from the tumor center **(A, C)** after 5hrs **(B, D)** after 9 hrs, for 100 nm diameter of vascular pore size and 7.5×10^{-14} $m^2(Pa\ s)^{-1}$ hydraulic conductivity of the tumor interstitial space, and for different drug diameter: **(A, B)** 20 nm and **(C, D)** 60nm.
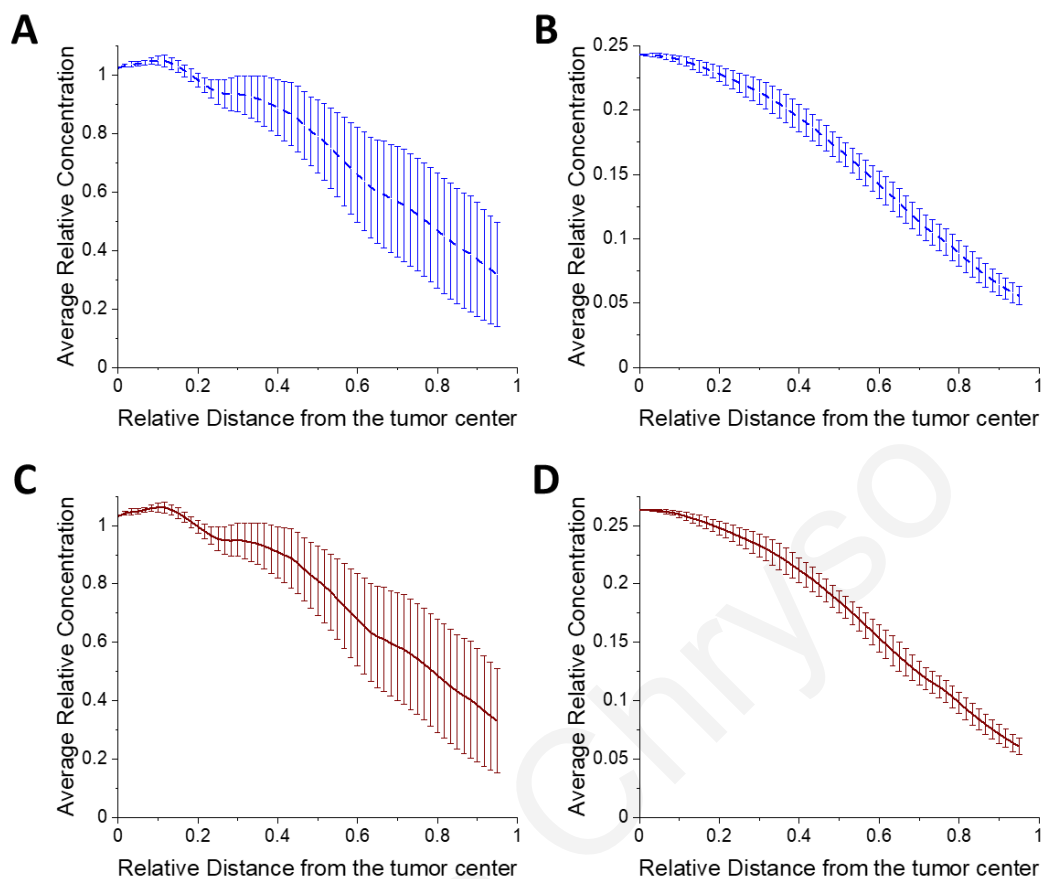
Figure 6: Plots of the average relative concentration calculated from the four directions as a function of the relative distance from the tumor center **(A, C)** after 5hrs **(B, D)** after 9 hrs, for 100 nm diameter of vascular pore size and 7.5×10^{-13} m^2(Pa s)$^{-1}$ hydraulic conductivity of the tumor interstitial space, and for different drug diameter: **(A, B)** 20 nm and **(C, D)** 60nm.
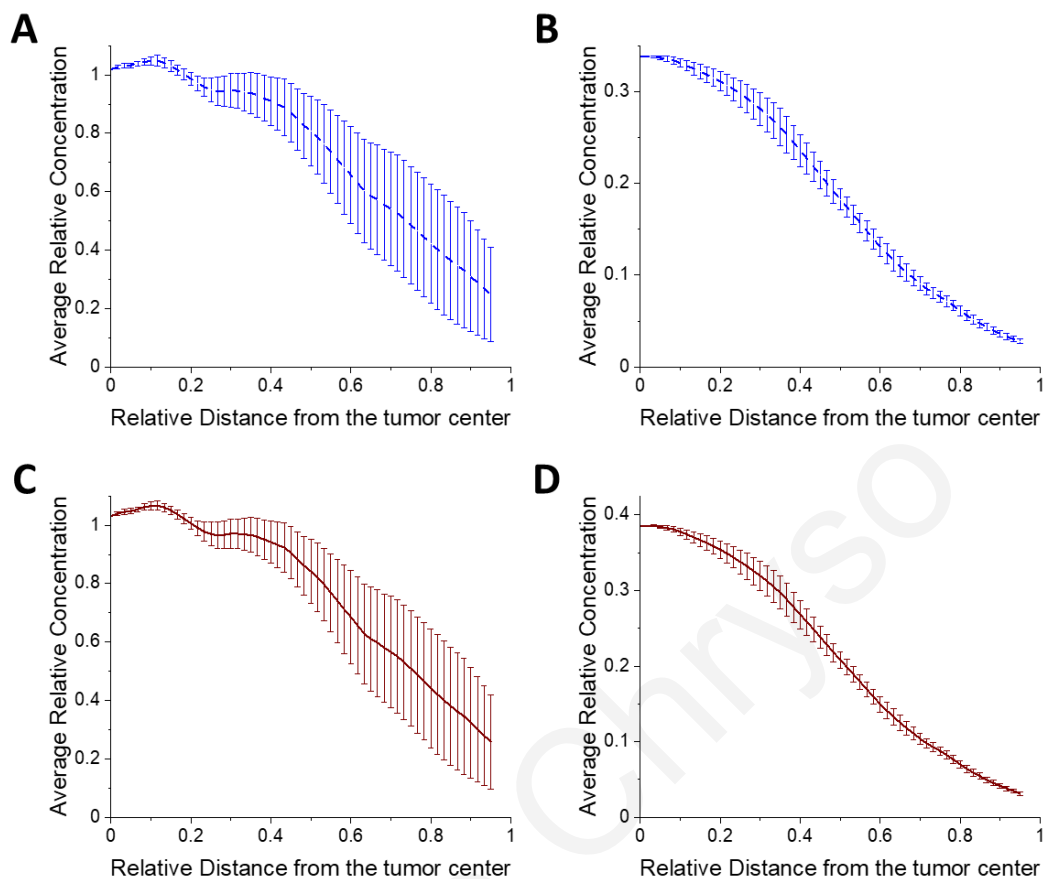
Figure 7: Plots of the average relative concentration calculated from the four directions as a function of the relative distance from the tumor center **(A, C)** after 5hrs **(B, D**) after 9 hrs, for 150 nm diameter of vascular pore size and 7.5×10^{-13} m^2(Pa s)$^{-1}$ hydraulic conductivity of the tumor interstitial space, and for different drug diameter: **(A, B)** 20 nm and **(C, D)** 60nm.